PHYSICAL REVIEW A **85**, 013817 (2012)

Dynamics of nonequilibrium Dicke models

M. J. Bhaseen,[1] J. Mayoh,[2,*] B. D. Simons,[1] and J. Keeling[2]
[1] *Cavendish Laboratory, University of Cambridge, Cambridge, CB3 0HE, United Kingdom*
[2] *School of Physics and Astronomy, University of St Andrews, St Andrews, KY16 9SS, United Kingdom*

(Received 6 October 2011; published 17 January 2012)

Motivated by experiments observing self-organization of cold atoms in optical cavities, we investigate the collective dynamics of the associated nonequilibrium Dicke model. The model displays a rich semiclassical phase diagram of long-time attractors including distinct superradiant fixed points, bistable and multistable coexistence phases, and regimes of persistent oscillations. We explore the intrinsic time scales for reaching these asymptotic states and discuss the implications for finite-duration experiments. On the basis of a semiclassical analysis of the effective Dicke model, we find that sweep measurements over 200 ms may be required in order to access the asymptotic regime. We briefly comment on the corrections that may arise due to quantum fluctuations and states outside of the effective two-level Dicke model description.

DOI: 10.1103/PhysRevA.85.013817 PACS number(s): 37.30.+i, 42.50.Pq

I. INTRODUCTION

In recent years there has been rapid progress in controlling the behavior of ultracold atoms using a wide variety of optical techniques. This includes confining atoms in optical traps and optical lattice potentials in conjunction with tremendous advances in laser cooling. More recently it has become possible to study the properties of Bose-Einstein condensates (BECs) in ultrahigh-finesse optical cavities [1]. Closely related experiments have also been performed on novel hybrid systems combining optical fibers on atom chips [2–4]. A central feature of these experiments is that one may access the strongly coupled regime of cavity quantum electrodynamics (QED). In this regime a large number of atoms, N, exchange photons many times on the time scale set by cavity leakage. This permits the exploration of coherent matter-light interactions and the observation of the collective $\sqrt{N}$ splitting of the resulting eigenstates. It also leads to novel forms of collective dynamics and cavity optomechanics [5–8]. Moreover, the light leaving the cavity provides valuable information on strongly correlated phases [9–12], thereby fostering links between contemporary problems in cold atomic gases, quantum optics, and condensed matter physics. These systems also offer exciting possibilities as matter-light interfaces for quantum-information processing. This wealth of activity is further stimulated by pioneering circuit QED experiments [13,14], which include direct observations of Berry phases [15], vacuum fluctuations [16], collective behavior [17,18], and three-qubit entanglement [19].

An important aspect of these developments is the potential for novel phases and phase transitions induced by the cavity light field. The latter mediates long-range interactions between the atoms which may strongly influence their behavior. It was recently predicted that an atomic cloud with additional transverse pumping undergoes a self-organization transition to a spatially modulated phase [20]; see Fig. 1. This was confirmed experimentally by Vuletić and co-workers using thermal clouds in an optical cavity [21]. Above a critical pumping strength the atoms self-organize to form a checkerboard pattern, as illustrated in Fig. 1. This dynamically generated lattice leads to a strong enhancement of the cavity light field due to coherent Bragg scattering. Heterodyne measurements of the phase of the cavity output also reveal the discrete $\mathbb{Z}_2$-symmetry breaking of the emergent lattice. More recently, this self-organization phenomenon was investigated experimentally using a BEC in an optical cavity [22,23]. In this setup spontaneous sublattice symmetry breaking coexists with superfluid phase coherence, giving rise to a novel form of supersolid [24–26]. In addition it was pointed out that this self-organization transition is a dynamical version of the superradiance transition in the Dicke model [22,23,27]. The Dicke model [28–32] has a long history and describes two-level systems or "spins" uniformly coupled to light. When the matter-light coupling exceeds a critical value, the Dicke model exhibits a continuous phase transition to a state with a nonvanishing photon population and discrete parity symmetry breaking; for a review of the Dicke model and its applications in quantum optics, see Ref. [33].

In the present cold-atom setting the effective Dicke model spin states are two distinct momentum states of the BEC [22,23]. Their splitting is therefore controlled by the atomic recoil energy, and this enables the Dicke model transition to be observed using light with optical frequencies. This approach is a close analog of an elegant theoretical proposal by Dimer *et al.* [34] for realizing the Dicke model transition using a Raman pumping scheme between distinct hyperfine states. These atomic experiments also provide a direct implementation of a Dicke model Hamiltonian without any additional diamagnetic terms. This circumvents the usual no-go theorems for observing the superradiance transition [35–37]. The experiments also have close connections to work on the collective atomic recoil laser (CARL) [38–40]. For further work on self-organized matter-light systems and the possibility of novel phases and phase transitions in multimode cavities, see Refs. [41–49].

A crucial feature of the cavity superradiance experiments is that they are concerned with intrinsically open systems with strong pumping and large cavity loss rates [22,23]. Any account of their physical properties therefore requires

---

[*] Present address: University of Cambridge, Cavendish Laboratory, Cambridge, CB3 0HE, UK.

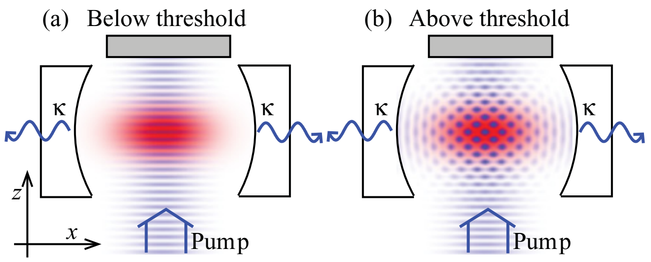

FIG. 1. (Color online) Experimental setup showing cold atoms (red) in an optical cavity with transverse pumping [20–23]. (a) Below the threshold pump power only the pump mode is present. (b) Above the threshold the atoms self-organize into a checkerboard lattice and are trapped in the interference pattern of the pump and cavity beams. The self-organization transition for a BEC is described by the onset of superradiance in an effective nonequilibrium Dicke model.

a nonequilibrium approach. Motivated by this experimental situation, we recently explored key aspects of the collective dynamics of BECs in optical cavities [50]. On the basis of a semiclassical analysis of the generalized Dicke model presented in Refs. [22,23], we obtained a surprisingly rich phase diagram of nonequilibrium phases and phase transitions. Most interestingly, we have found that the open system displays two significant features. First, for the parameters used in the recent experiments we find additional attractors of the long-time dynamics that have *not* yet been seen in experiment. In particular, the experiment suggests a normal state without photons, in a region where the semiclassical analysis predicts that the normal state is unstable. Second, we find a rich array of phases in experimentally unexplored regions of the phase diagram. This includes coexistence phases and regimes of persistent oscillations. The aim of this present paper is to shed further light on these pertinent issues and to develop deeper links between theory and experiment. To this end, we explore the semiclassical collective dynamics with a specific emphasis on the emergent time scales and the observability of the characteristic features. A key finding is that these time scales vary quite considerably throughout the phase diagram. Under the assumption that the effective Dicke model fully describes the experimental system [22,23] our primary conclusion is that the $O(10\ \text{ms})$ duration of the current experiments may not be sufficient to reach the long-time asymptote in all cases. We discuss the prospects for observing the predicted asymptotic states in longer-duration experiments and in other realizations of the nonequilibrium Dicke model. We also discuss the possible role of quantum fluctuations and states outside of the effective Dicke model description.

The layout of this paper is as follows. In Sec. II we provide an introduction to the recent experiments [22,23] and the associated Dicke model. In Sec. III we discuss the semiclassical dynamics of this inherently open nonequilibrium system. In Sec. IV we present the dynamical phase diagram for the presently available experimental parameters and discuss the nature of the long-time attractors and the associated time evolution. In Sec. V we investigate the characteristic time scales governing the initial and final stages of the collective dynamics and discuss the implications for finite-duration experiments. In Sec. VI we investigate the phase diagram for a broader range of parameters and discuss the appearance of persistent oscillations. In Sec. VII we examine the effects of contributions which go beyond the effective Dicke model and its semiclassical treatment. We conclude in Sec. VIII and provide directions for further research. We also include technical Appendixes addressing the derivation of the effective Dicke model, and the location of fixed points and their linear stability properties. We also provide further details on the phase diagram. In order to make the paper self-contained we incorporate some of the principal findings of our previous Letter [50].

II. EXPERIMENT AND NONEQUILIBRIUM GENERALIZED DICKE MODEL

The experiment of Ref. [22] consists of an ^{87}Rb BEC with approximately $N = 10^5$ atoms prepared in their motional ground state with $|k_x,k_z\rangle = |0,0\rangle$. The atoms are placed in an ultrahigh-finesse optical cavity of length 178 μm and cavity loss rate $\kappa = 8.1$ MHz. As shown in Fig. 1 the BEC is subjected to a transverse pump beam with Rabi frequency Ω_p, wave vector k, and frequency ω_p. The latter is far detuned from the atomic transition frequency ω_a, in order to avoid population of this excited level. One may therefore neglect the effects of spontaneous emission. However, the pump frequency is near detuned to the cavity frequency ω_c, resulting in efficient scattering from the pump beam into the cavity, and vice versa. The coupling strength of a single atom to the cavity mode is denoted by g_0, and the corresponding level scheme is shown in Fig. 2. The experiment is a close analog of a theoretical proposal by Dimer *et al.* [34] for realizing the Dicke model by using Raman pumping to couple to two ground-state hyperfine

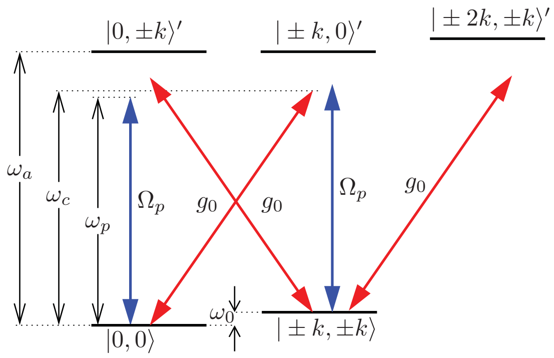

FIG. 2. (Color online) Level scheme corresponding to the experimental setup shown in Fig. 1. The pump beam has frequency ω_p, wave vector k, and Rabi frequency Ω_p. The strength of the cavity coupling is given by g_0. The frequencies of the cavity and the atomic transition are denoted by ω_c and ω_a, respectively. Here $|k_x,k_z\rangle$ are momentum states of the atoms in the BEC, and excited electronic states are denoted by a prime. The atomic ground state with $|k_x,k_z\rangle = |0,0\rangle$ and the symmetric superposition labeled as $|\pm k, \pm k\rangle$ constitute an effective two-level system governed by an effective nonequilibrium Dicke model. The corresponding level splitting is given by $\omega_0 = 2\omega_r$, where $\omega_r = \hbar^2 k^2/2m$ is the atomic recoil energy resulting from the absorption or emission of a single photon. In general, multiphoton processes are required in order to couple the ground state to higher-momentum states.

levels. A notable difference is that the present experiment exploits a Rayleigh scheme, involving distinct momentum states rather than internal hyperfine states. This generically leads to the presence of a back-reaction term, discussed below, which may be avoided in the proposal of Ref. [34].

Absorption and emission of photons yields an effective two-level spin system [22,27] where spin down corresponds to the ground state $|0,0\rangle$, and spin up corresponds to the excited momentum state $|\pm k, \pm k\rangle \equiv \frac{1}{2}\sum_{\alpha,\beta=\pm}|\alpha k,\beta k\rangle$. The latter denotes the symmetric superposition of momentum states resulting from two-photon emission and absorption processes with $k_x,k_z \in \{\pm k\}$. In this basis one may introduce collective spin raising operators $S^+ = \sum_{i=1}^{N} |\pm k, \pm k\rangle_{i\ i}\langle 0,0|$ where i labels the atoms and S^- is obtained by Hermitian conjugation. The quantum dynamics of this inherently open system, with a large cavity loss rate κ, can be described by the density matrix equation in Lindblad form [51],

$$\partial_t \rho = -i[H,\rho] - \kappa(\psi^\dagger\psi\rho - 2\psi\rho\psi^\dagger + \rho\psi^\dagger\psi), \qquad (1)$$

where ρ is the system density matrix, ψ is the cavity photon mode annihilation operator, and t denotes time.[1] The effective Hamiltonian H takes the form of a generalized Dicke model with [22,27,34]

$$\begin{aligned} H = {} & \omega\psi^\dagger\psi + \omega_0 S_z + U S_z \psi^\dagger\psi + g(\psi^\dagger S^- + \psi S^+) \\ & + g'(\psi^\dagger S^+ + \psi S^-), \end{aligned} \qquad (2)$$

where $\mathbf{S} = (S_x,S_y,S_z)$ is the effective collective spin of length $N/2$ and $S^\pm = S_x \pm i S_y$. The derivation of Eq. (2) from the microscopic description, together with a discussion of higher-order contributions, is given in Appendix A. For weak pumping, and in the limit that the atom-cavity detuning is much larger than both the pump-cavity detuning and the recoil energy [22,23], the coefficients are given by $\omega = \omega_c - \omega_p - N(5/8)g_0^2/(\omega_a - \omega_c)$ and $\omega_0 = 2\omega_r$, where $\omega_r = \hbar^2k^2/2m$ is the atomic recoil energy. The term involving $U = -(1/4)g_0^2/(\omega_a - \omega_c)$ describes the back reaction of the cavity light field on the BEC, and may be interpreted as the ac Stark shift due to the appearance of a weak optical lattice in the cavity. In the experiment [22], both the pump and the cavity are red detuned from the atomic transition, so U is negative. However, both signs of U are physically achievable. In the atomic ground state, the effective cavity frequency $\omega_{\text{eff}} = \omega + US_z$ is given by $\omega_{\text{eff}} = \omega - UN/2 = \omega_c - \omega_p - Ng_0^2/2(\omega_a - \omega_c)$,[2] in agreement with Ref. [22]. The Hamiltonian (2) contains both co- and counter-rotating matter-light couplings denoted by g and g', respectively. In the large atom-pump detuning limit relevant to the experiment [22], one may write $g = g' = g_0\Omega_p/2(\omega_p - \omega_a)$.

For the experimental parameters used in Ref. [22], $\omega_0 = 0.047$ MHz and $UN = -6.5\kappa/4 = -13.3$ MHz, where the latter is inferred from the observed dispersive shift of the cavity frequency, $\omega_{\text{eff}} = \omega_c - \omega_p + 2UN$.[3] In the subsequent discussion we will endeavor to place these experiments in a broader context, and without loss of generality we will approximate these conditions as $\omega_0 \approx 0.05$ MHz and $UN \approx -10$ MHz; note that the latter differs from the value taken in our previous Letter [50] due to a small discrepancy in the reported Hamiltonian in Ref. [22]. Specifically, the Hamiltonian given in Eq. (2) differs from Eq. (4) of Ref. [22] due to a discrepancy in the indicated matrix element $M = 3/4$ in the notation of Ref. [22]. This does not affect the location of the reported superradiance transition, but is important for establishing the broader phase diagram. In addition to the energy and time scales appearing in the model described by Eqs. (1) and (2), there is a limit on the duration of current experiments which is set by the rate of atom loss. In the initial experiments [22] this was of the order of 100 ms, but is notably longer in subsequent experiments [23].

III. SEMICLASSICAL DYNAMICS OF THE OPEN SYSTEM

Having discussed the effective Hamiltonian and the density matrix equation of motion in Sec. II, we now turn to discuss the dynamics arising from this model. This is essential in order to interpret time-dependent nonequilibrium experiments performed in an open cavity [22,23]. In view of the large number of atoms comprising the Dicke model spin states, we will first consider the semiclassical limit of this dynamics [50]. In Sec. VII we will briefly comment on the role of quantum fluctuations.

A. Equations of motion and symmetries

The semiclassical equations of motion for the open system described by Eqs. (1) and (2) are given by

$$\begin{aligned} \dot{S}^- &= -i(\omega_0 + U|\psi|^2)S^- + 2i(g\psi + g'\psi^*)S_z, \\ \dot{S}_z &= -ig\psi S^+ + ig\psi^* S^- + ig'\psi S^- - ig'\psi^* S^+, \\ \dot{\psi} &= -[\kappa + i(\omega + US_z)]\psi - igS^- - ig'S^+, \end{aligned} \qquad (3)$$

where $S^\pm \equiv S_x \pm iS_y$, κ is the cavity loss rate, and we neglect the effects of atom loss [22]. The Hamiltonian in Eq. (2) conserves the total length of the collective spin since $[\mathbf{S}^2, S_\alpha] = 0$ for $\alpha = x,y,z$. Likewise, Eq. (3) satisfies $\partial_t \mathbf{S}^2 = 0$ for all κ. As such, the dynamics can be explored on the Bloch sphere with $|\mathbf{S}| = N/2$. In addition to this conservation law there are further discrete symmetries. In particular, the equations of motion in Eq. (3) are invariant under the parity transformation

$$\psi \to -\psi, \quad S^\pm \to -S^\pm, \qquad (4)$$

as in the equilibrium Dicke model. This symmetry is spontaneously broken on passing from the normal phase with $\psi = 0$ to the superradiant phase with $\psi \neq 0$ [22,23]. The equations of motion are also invariant under the combined variable and parameter change

$$\mathbf{S} \to -\mathbf{S}, \quad \psi \leftrightarrow \psi^*, \quad \omega \to -\omega, \quad g \leftrightarrow g'. \qquad (5)$$

---

[1] In these notations the rate of loss of energy is 2κ.

[2] In the notations of Ref. [22], the effective cavity frequency ω_{eff} is denoted by ω.

[3] In the experiment [22], the spatial overlap of the cavity mode profile and atomic density is not perfect, and so this feedback term is reduced slightly from this ideal value.

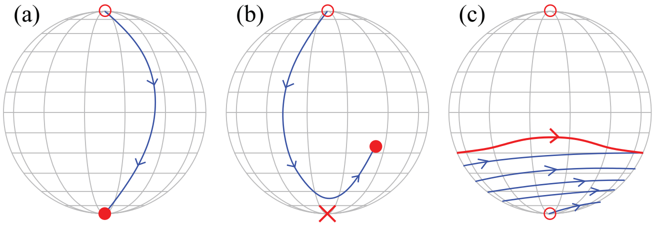

FIG. 3. (Color online) Schematic illustration of the different types of behavior displayed by the semiclassical equations of motion in Eq. (3), for trajectories on the Bloch sphere with $|\mathbf{S}| = N/2$. (a) Evolution from an unstable fixed point (open circle) to a stable attractor (closed circle) of the long-time dynamics for all initial conditions. Both the stable and unstable points have $\dot{\mathbf{S}} = \mathbf{0}$ and $\dot{\psi} = 0$. However, for the stable attractor small perturbations decay, while for the unstable fixed point fluctuations grow. (b) As for (a) but with a hyperbolic fixed point (cross) having one stable and one unstable eigenmode. Paths first approach and then leave the vicinity of this hyperbolic point, before eventually reaching a stable attractor with $\dot{\mathbf{S}} = \mathbf{0}$ and $\dot{\psi} = 0$. (c) Dynamics exhibiting a stable limit cycle with $\dot{\mathbf{S}} \neq \mathbf{0}$ and $\dot{\psi} \neq 0$ for all initial conditions.

As we shall see in Sec. III B, both the symmetry in Eq. (4) and the duality relation in Eq. (5) will have a direct manifestation on the Bloch sphere portraits; the attractors are related by these discrete transformations.

In order to get a full understanding of the behavior of Eq. (3), it is necessary to address two questions. The first regards the nature of the long-time attractors. The second concerns the full time evolution and its connection to the asymptotics. The former is important because there are fundamental differences between the dynamical phase diagram of the open system and the equilibrium phase diagram of the Hamiltonian; even for $\kappa \to 0$ these are generically distinct. The latter question is crucial because the open-cavity experiments have a finite duration and may not always reach the long-time asymptote.

For most values of the parameters, the long-time asymptotes are steady states and may be identified as stable fixed points. That is to say, for these parameters there are values of $\mathbf{S}$ and ψ for which $\dot{\mathbf{S}} = \mathbf{0}$ and $\dot{\psi} = 0$, and these steady states are the eventual fate of the semiclassical dynamics for all initial conditions. We will therefore discuss what these steady states are, and where possible give analytical formulas for them. In the following sections we will then use this information to present dynamical phase diagrams, describing which stable fixed points exist for different values of the parameters. We will then address the dynamical bifurcations that correspond to the phase boundaries, as well as addressing those cases where the long-time asymptotes are more complicated than steady states, such as persistent oscillations. We illustrate these possibilities in Fig. 3.

Before discussing the semiclassical equations of motion in Eq. (3), let us comment on some known limiting cases that have been studied in the literature. With $\kappa = 0$, $g' = 0$, and $U = 0$, these equations correspond to the semiclassical dynamics of the equilibrium Dicke model without the loss of photons and without counter-rotating terms [52]. This model arises in various contexts and has recently been discussed in relation to nonequilibrium Cooper pairing [53–56]. In this setting, the constituent fermions are modeled by Anderson pseudospins [57], and the cavity light field ψ corresponds to the closed molecular channel. A key finding of these studies is the presence of collective oscillations. This may also be seen by exploiting the integrability of the closely related BCS (Bardeen-Cooper-Schrieffer) Hamiltonian [55,56]. The same equations of motion also apply to polariton condensation and the synchronization of oscillators [58,59]. Quantum corrections to this collective dynamics have also been explored in Refs. [60,61].

In contrast to the case when $g' = 0$, when $\kappa = 0$, $g = g'$, and $U = 0$, the equilibrium Dicke model is no longer integrable. Nonetheless, the model is tractable in the thermodynamic limit and displays a mean-field superradiance transition. Strikingly, the energy levels reveal a crossover from Poisson statistics to Wigner statistics in the vicinity of the critical coupling [31,32]. This indicates the onset of quantum chaos and is accompanied by chaotic attractors in the analogous classical dynamics.

More recently, Dimer *et al.* [34] have proposed a novel scheme for realizing the nonequilibrium Dicke model described by Eqs. (1) and (2) with $\kappa \neq 0$. The parameters in this effective model are readily adjustable and they focus on the particular case with $g = g'$ and $U = 0$. A notable observation is that cavity losses lead to a shift of the mean-field superradiance transition, in agreement with recent experiments with $U \neq 0$ [22,23,27].

It is evident from this survey of limiting cases that rich collective dynamics is expected to emerge for the more general system of equations given by Eq. (3) and in open-cavity experiments. We shed light on this below.

B. Fixed-point attractors

In order to get a handle on the possible long-time steady states, we first enumerate the solutions of the equations of motion with $\dot{\mathbf{S}} = \mathbf{0}$ and $\dot{\psi} = 0$. These fixed-point solutions may be either stable or unstable, and we postpone a discussion of their stability properties until Sec. III C. It is readily verified that the normal state ($\Downarrow$) is always a possible steady-state solution with all the spins pointing down, $S_z = -N/2$, and no photons, $\psi = 0$. Likewise, so is the inverted state ($\Uparrow$) with all the spins pointing up, $S_z = N/2$, and no photons, $\psi = 0$. More generally one may look for nontrivial solutions with a nonvanishing photon population and a nontrivial magnetization S_z. To find these configurations we first note that a steady-state solution satisfying the first equation in Eq. (3) automatically satisfies the second equation. As such Eq. (3) reduces to a pair of complex equations. Denoting $\psi = \psi_1 + i\psi_2$ and $S^{\pm} = S_x \pm iS_y$, one obtains

$$\begin{aligned}\left[\omega_0 + U\left(\psi_1^2 + \psi_2^2\right)\right](S_x - iS_y) \\ = 2[(g+g')\psi_1 + i(g-g')\psi_2]S_z\end{aligned} \tag{6}$$

and

$$[\kappa + i(\omega + US_z)](\psi_1 + i\psi_2) = -i(g+g')S_x - (g-g')S_y. \tag{7}$$

In general these equations may be difficult to solve analytically. However, simplifications occur when $U = 0$ or when $g = g'$. We focus here on the latter since the experiments of Ref. [22]

correspond to $g = g'$ and negative U. We discuss the behavior for $g \neq g'$ in Appendix B.

With $g = g'$, the fixed-point equations (6) and (7) read

$$(\omega_0 + U|\psi|^2)S_x = 2g(\psi + \psi^*)S_z, \tag{8a}$$

$$(\omega_0 + U|\psi|^2)S_y = 0, \tag{8b}$$

$$(\omega + US_z - i\kappa)\psi = -2gS_x. \tag{8c}$$

It follows from Eq. (8b) that there are two classes of solution depending on whether $S_y = 0$ or $\omega_0 + U|\psi|^2 = 0$. We consider these two classes in turn and refer to the nontrivial steady-state solutions as superradiant A (SRA) and B (SRB), respectively. Assuming $\omega_0 > 0$, for $U \geqslant 0$ only the first type, the SRA solution, may be present. This solution corresponds to the familiar superradiant phase in the usual Dicke model where $U = 0$. For $U < 0$ the second type, the SRB solution, may exist [50]. As we shall discuss below, in general these solutions are continuously connected in the broader parameter space with $g \neq g'$. Nonetheless, it is important to distinguish between these distinct solutions of the steady-state equations of motion when $g = g'$. We will discuss the experimental consequences of this distinction in Secs. IV and V.

1. *Superradiant A steady states*

Equation (8c) may be rearranged as an equation for ψ and substituted into Eq. (8a):

$$\omega_0(\omega + US_z)^2 + \omega_0\kappa^2 + 4g^2US_x^2 = -8g^2(\omega + US_z)S_z, \tag{9}$$

where we have canceled a factor of $S_x \neq 0$ from both sides of the equation. Using the fixed-length spin constraint $S_x^2 = N^2/4 - S_z^2$, one obtains a quadratic equation for S_z. This may be solved to yield [50]

$$\frac{S_z}{N} = -\frac{\omega}{UN} \pm \sqrt{\frac{g^2N[4\omega^2 - (UN)^2] - \omega_0 UN\kappa^2}{(UN)^2(\omega_0 UN + 4g^2N)}}, \tag{10}$$

where the accompanying steady-state photon population follows from Eq. (8c). In general only one of these roots corresponds to a physical solution with $|\mathbf{S}| \leqslant N/2$. However, as we shall discuss in Sec. IV B and Appendix D, there are regions of parameter space where both roots of Eq. (10) are supported; see the regions denoted 2SRA in Figs. 5 and 17. In addition, there are two possible signs for $S_x = \pm\sqrt{N^2/4 - S_z^2}$, where the associated sign of ψ is determined by Eq. (8c). This sign choice corresponds to the parity symmetry in Eq. (4) which is spontaneously broken at the superradiance transition.

The critical coupling strength corresponding to the onset of superradiance starting from the normal ($\Downarrow$) or inverted state ($\Uparrow$) is obtained by setting $\mathbf{S} = (0,0,\mp N/2)$ in Eq. (9). One obtains

$$g_a^{\mp}\sqrt{N} = \sqrt{\pm\frac{\omega_0(\omega_{\mp}^2 + \kappa^2)}{4\omega_{\mp}}}, \tag{11}$$

where $\omega_{\mp} \equiv \omega \mp \omega_u$ and $\omega_u \equiv UN/2$. It is readily seen from the Hamiltonian (2) that $\omega_{\mp}$ plays the role of an effective cavity frequency for the normal and inverted states, respectively. For the special case where $U = 0$ this agrees with the results of Dimer *et al.* [34]. In the additional limit $\kappa = 0$, Eq. (11) reproduces the location of the superradiance transition, $g\sqrt{N} = \sqrt{\omega\omega_0}/2$, for the equilibrium Dicke model with counter-rotating terms. More generally, Eq. (11) gives the onset of the SRA phase in the open-cavity system with transverse pumping and $g = g'$, as recently confirmed experimentally [22]. The explicit dependence on κ of the phase boundary in Eq. (11) emphasizes the open character of the experimental system.

2. *Superradiant B steady states*

For negative U it is evident from Eq. (8b) that another class of solutions may be obtained if $\omega_0 + U|\psi|^2 = 0$. Equation (8a) may thus be fulfilled by taking ψ to be purely imaginary. It then follows from Eq. (8c) that $\omega + US_z = 0$. This yields [50]

$$\psi = \pm i\sqrt{-\frac{\omega_0}{U}}, \quad S_z = -\frac{\omega}{U}, \quad S_x = \mp\frac{\kappa}{2g}\sqrt{-\frac{\omega_0}{U}}, \tag{12}$$

where the magnitude of S_y follows from the normalization condition $\mathbf{S}^2 = N^2/4$. In order to obtain real solutions for S_y, we require $S_x^2 + S_z^2 \leqslant N^2/4$. This is equivalent to the condition $g \geqslant g_b$ where

$$g_b\sqrt{N} = \kappa\sqrt{\frac{\omega_0\omega_u}{2(\omega^2 - \omega_u^2)}}. \tag{13}$$

In order to yield $|S_z| < N/2$ we require $|\omega| < |\omega_u|$. In contrast to the SRA solution which may exist for either sign of U depending on the parameters, the functional dependence in Eq. (12) clearly indicates that the SRB solution exists only for $U < 0$. In the special case where $g = g_b$ and $S_y = 0$, the SRA and SRB solutions coincide.

In conjunction with both possible signs for $S_y = \pm|S_y|$, Eq. (12) defines four distinct steady states. These divide into two pairs of solutions, where the pairs of solutions are related by the discrete parity symmetry in Eq. (4). As we shall see in Sec. IV B, two of these four solutions correspond to stable attractors of the long-time dynamics while the other two solutions correspond to unstable fixed points; see Fig. 6(d).

C. Linear stability of fixed points and more exotic attractors

In Sec. III B we discussed the possible fixed points of the equations of motion with $\dot{\mathbf{S}} = \mathbf{0}$ and $\dot{\psi} = 0$. Here we turn our attention to the linear stability of these fixed points as potential candidates for the long-time attractors. The calculations are most transparent if we consider the instability of the normal ($\Downarrow$) and inverted states ($\Uparrow$) where $\psi = 0$ and $S_z = \mp N/2$, respectively. For arbitrary fixed points the approach is readily generalized but is algebraically more involved; the details are outlined in Appendix C. Writing $\psi = \psi_0 + \delta\psi$ and $S^- = S_0^- + \delta S^-$ where $\psi_0 = 0$, $S_0^- = 0$, and $S_z = \mp N/2$, and substituting into Eq. (3), one obtains the linearized equations

$$\begin{aligned} \delta\dot{S}^- &= -i\omega_0\delta S^- \mp igN\delta\psi \mp ig'N\delta\psi^*, \\ \delta\dot{\psi} &= -(\kappa + i\omega_{\mp})\delta\psi - ig\delta S^- - ig'\delta S^+, \end{aligned} \tag{14}$$

where $\dot{S}_z = 0$, $\omega_{\mp} \equiv \omega \mp \omega_u$, and $\omega_u \equiv UN/2$. Parametrizing $\delta\psi = ae^{-i\eta t} + b^*e^{i\eta^* t}$ and $\delta S^- = ce^{-i\eta t} + d^*e^{i\eta^* t}$ and equating coefficients with the same time dependence, one obtains

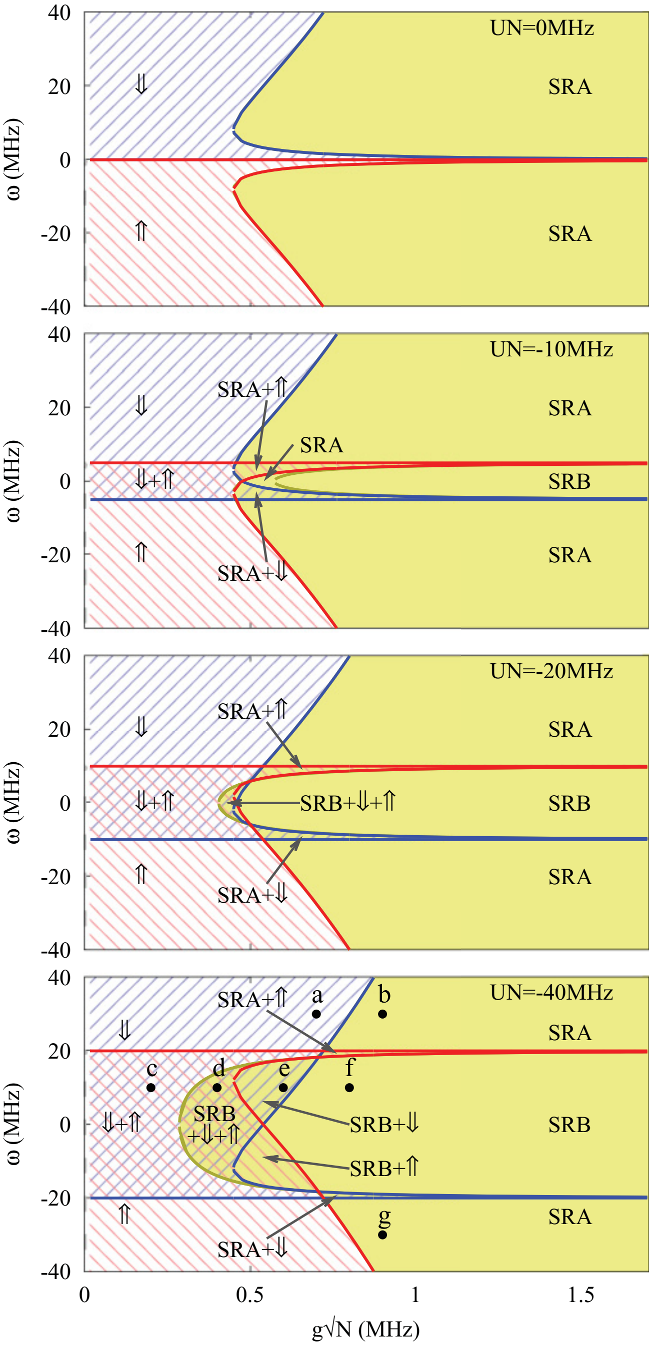

FIG. 4. (Color online) Dynamical phase diagram of the stable attractors as a function of the cavity frequency ω and the coupling $g = g'$ with parameters $\kappa = 8.1$ MHz and $\omega_0 = 0.05$ MHz taken from Ref. [22]. The panels represent different values of the feedback term U, going from $U = 0$ (top) to $UN = -40$ MHz (bottom). The second panel corresponds to the experimental parameters used in Ref. [22]. Points (a)–(f) marked in the bottom panel correspond to the fixed-point illustrations shown in Fig. 6. The characteristic time evolution at points (b), (f), and (g) is given in Figs. 7 and 8.

algebraic equations for a, b, c, and d. The self-consistency equations characterize the possible instabilities and are given by Eqs. (C1) and (C2). In the case where $g = g'$ the frequencies η satisfy

$$\left(\eta^2 - \omega_\mp^2 - \kappa^2\right)\left(\eta^2 - \omega_0^2\right) \mp 4g^2 N\omega_\mp\omega_0 - 2i\kappa\eta\left(\eta^2 - \omega_0^2\right) = 0. \qquad (15)$$

The dividing line between exponentially growing and decaying fluctuations corresponds to Eq. (15) having real solutions for η. In this case the imaginary part of Eq. (15) vanishes when either $\eta = 0$ or $\eta^2 = \omega_0^2$. Demanding that the real part of Eq. (15) vanishes when $\eta = 0$ yields Eq. (11). That is to say, the normal and inverted states become unstable at precisely the same point where the SRA state becomes possible. For $g \geqslant g_a^\mp$, Eq. (15) has one unstable root, and in the language of dynamical phase transitions this corresponds to a pitchfork bifurcation. In the case of frequencies satisfying $\eta^2 = \omega_0^2$ the real part of Eq. (15) vanishes when $\omega_\mp = 0$. This implies that the normal and inverted states also become unstable when $\omega = \pm UN/2$, respectively. For values of ω beyond these points, Eq. (15) develops two unstable roots, and the dynamical phase transition corresponds to a Hopf bifurcation. As we shall see in Secs. IV and VI, all of these instabilities describe boundaries in the emergent dynamical phase diagrams shown in Figs. 4 and 13.

In the above analysis we have outlined the existence of various fixed points and briefly discussed their linear stability properties. These considerations are essential because more than one of these fixed points may exist at a given point in parameter space. For example, the normal (⇓) and inverted (⇑) fixed points always exist, possibly as unstable fixed points, even in the presence of the superradiant solutions. As we shall see in Sec. IV, there are in fact cases where more than one stable fixed point exists at a given point in parameter space. In addition to these coexistence phases, where the final state depends on the initial conditions, it is also possible to find regions of parameter space where no stable fixed point exists. In these cases the system may be attracted to time-dependent solutions such as limit cycles, as found in other nonlinear dynamical systems. In the remainder of this paper we search for the complete set of stable attractors of the long-time dynamics, including fixed points, bistable and multistable coexistence phases, and time-dependent trajectories.

IV. DYNAMICAL PHASE DIAGRAM OF LONG-TIME ATTRACTORS FOR $g = g'$ AND $U < 0$

In the previous section we gave a brief overview of the simplest fixed-point attractors and their linear stability properties. In this section we build upon these results and establish the dynamical phase diagram corresponding to the semiclassical dynamics in Eq. (3). That is to say, we identify which stable long-time attractors exist at a given point in parameter space. In order to make contact with experiment [22,23], in this section we restrict our attention to $g = g'$ and $U < 0$. We begin in Sec. IV A by exploring the phase diagram as a function of the remaining parameters g, ω, and U, where the value of $\omega_0 = 0.05$ MHz is motivated by Ref. [22]. In Sec. IV B we then focus on different points in the dynamical phase diagram in order to clearly expose the nature of the underlying attractors, including their stability properties and their locations on the Bloch sphere. In Sec. IV C we then discuss the characteristic time evolution toward the stable asymptotic states, and we rationalize these findings using linear stability analysis. In some regimes of parameter space, the time evolution can be rather slow, and we characterize where this occurs. We discuss the significant implications of these regions of long-lived transients for finite-duration experiments in Sec. V.

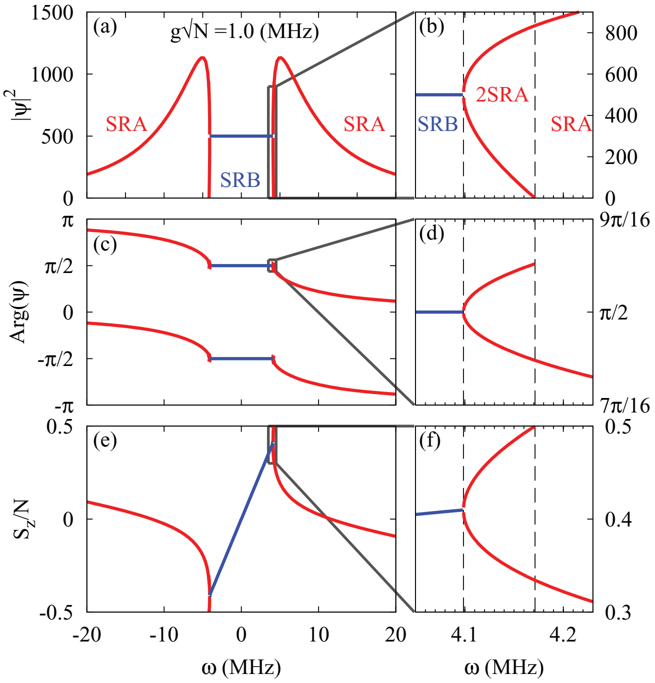

FIG. 5. (Color online) Vertical slice through the second panel of Fig. 4 with $UN = -10$ MHz, corresponding to the experimental parameters used in Ref. [22]. Variation of (a) $|\psi|^2$, (c) Arg(ψ), and (e) S_z on passing from the SRA to the SRB phase. In the vicinity of both of these transitions there is a narrow region of bistability denoted as 2SRA, where both of the SRA solutions given in Eq. (10) coexist; see (b), (d), and (f) for magnified images of the highlighted regions.

A. Phase diagram of asymptotic stable attractors

As discussed in Sec. II, the experiments of Ref. [22] are performed with $\omega_0 \simeq 0.05$ MHz, $\kappa = 8.1$ MHz, $UN \simeq -10$ MHz, and $g = g'$. We therefore summarize the dynamical phase diagram with these parameters. In order to provide some orientation, we illustrate how this phase diagram relates to that for the open Dicke model with $U = 0$, as a function of ω and g. We consider fixed values of the feedback term U, starting from the simplest possible case with $U = 0$, and decrease this parameter through the experimental value; see Fig. 4.

In this nonequilibrium setting, each phase is labeled according to the complete set of stable long-time attractors of the semiclassical dynamics given in Eq. (3). That is to say, the phase diagram corresponds to starting the system in a wide variety of initial conditions and examining the totality of stable end points. In this respect, the phase boundaries should be thought of as dynamical phase transitions, which separate distinct regimes of asymptotic behavior. In particular, the blue and red boundaries in Fig. 4 correspond to the instability of the normal ($\Downarrow$) and inverted ($\Uparrow$) states, respectively, and are given by Eq. (11), while the accompanying horizontal segments correspond to $\omega_\mp = 0$. The gold phase boundary indicates the critical coupling for the onset of the SRB phase and is given by Eq. (13). It is important to emphasize that, while all of these dynamical phase boundaries may be investigated experimentally, not all of them will emerge in a given experiment; the relevant phase boundaries are determined by the initial conditions. In particular, the experiments performed so far all begin in the normal state ($\Downarrow$) with no photons [22,23]. However, this is not a fundamental experimental restriction, and it is essential to survey the totality of attractors for all initial conditions, before considering particular initial states.

For $U = 0$ and $\omega > 0$, the structure of Fig. 4 mirrors the equilibrium phase diagram of the Dicke model, having a transition from a phase at low g where only the normal state ($\Downarrow$) is possible, to a phase where only the SRA state occurs. In the terminology of dynamical systems, this particular dynamical phase transition occurs via a pitchfork bifurcation at $g\sqrt{N} = \sqrt{\omega_0(\omega^2 + \kappa^2)/4\omega}$ [34]; a pair of superradiant fixed points emerge when the normal state loses stability. This parallels the situation in the equilibrium Dicke model where a pair of parity-related superradiant solutions emerges at a continuous phase transition. It is notable that as $\omega \to 0$, the critical value of g required for superradiance tends to infinity. This is because for $g = g'$ only the real part of ψ drives the polarization of the two-level system via the collective coupling $g(\psi + \psi^\dagger)(S^+ + S^-)$; as $\omega \to 0$, ψ becomes purely imaginary as may be seen from Eq. (3). In addition, for $\omega < 0$, the open dynamical system shows behavior that could not occur in thermal equilibrium; the normal state ($\Downarrow$) becomes unstable and the inverted state ($\Uparrow$) with $S_z = N/2$ and $\psi = 0$ is stable instead. It is evident from the Hamiltonian in Eq. (2) that the inverted state is of higher energy than the normal state. However, in contrast to the suggestions of Ref. [62], the relevant question for the experimental realization is dynamical stability, as opposed to minimum free energy. This behavior is directly confirmed by the duality of the equations of motion given in Eq. (5), and is reflected in the $\omega \to -\omega$ inversion symmetry of Fig. 4.

For negative U, the phase boundaries between the normal and inverted states and the SRA phase shift to lower and higher frequencies, respectively, in accordance with Eq. (11); see Fig. 4. This can be interpreted in terms of a state-dependent shift of the cavity frequency $\omega_\mp = \omega \mp \omega_u$, as suggested by the Hamiltonian (2) [20,42]. Within the region of overlap the SRB phase may be stabilized, as shown in Fig. 4. In particular, this results in a change in both the intensity and the phase of the cavity light field as indicated in Fig. 5. In addition, in the vicinity of these transitions between the SRA and SRB states, a narrow coexistence region emerges, denoted 2SRA, where both solutions of Eq. (10) are physical; see Appendix D. Indeed, such coexistence phases are abundant in the phase diagram shown in Fig. 4. For example, as a result of the effective frequency shifts induced by negative U, there is a region at low g where both the normal and inverted states coexist. More strikingly, for $UN < -2\kappa$ in this overlap region, there is an extension of the region of superradiant phases to lower g, so that the SRB fixed point can coexist with both the normal and the inverted states; see for example the point (d) in Fig. 4. In such a region, there are multiple possible stable attractors, and the ultimate fate of the system depends on the initial conditions. In particular, this will lead to multistability of the cavity output field. In addition, hysteresis can occur in these multistable regions. For example, increasing to a large value of g and then slowly reducing the value would lead to superradiant behavior at the point (d) shown in Fig. 4; in contrast, slowly increasing g from zero would allow the system to remain in the normal state for the same final parameters.

It is evident from the above discussion that the behavior of the open system is extremely rich and is fundamentally distinct from the equilibrium case with $\kappa = 0$. As emphasized above and in Ref. [50], the behavior of the open system is controlled by the stable attractors, which do not necessarily coincide with the points of minimal free energy. As such, there is a crucial distinction between the $\kappa \to 0$ limit of the dynamical system and the equilibrium behavior at $\kappa = 0$.[4] In order to address experiments with an open cavity one must consider time-dependent dynamics and $\kappa \neq 0$. In this setting, equilibrium concepts should only be applied with caution.

B. Nature of attractors

In the previous section we have considered the dynamical phase diagram with $g = g'$ and $U \leqslant 0$. Here, we provide a detailed discussion of the nature of the long-time attractors indicated in Fig. 4. We focus on the representative points (a)–(f) shown in Fig. 4, and chart the associated motion of the spins on the Bloch sphere with $|\mathbf{S}| = N/2$. In Fig. 6, we show the results obtained by numerical integration of the differential equations in Eq. (3), using an adaptive time step fourth-order Runge-Kutta routine from the Numerical Algorithms Group library [63]. In addition to the characteristic trajectories, in Fig. 6 we indicate the locations and nature of the various fixed points with $\dot{\psi} = 0$ and $\dot{\mathbf{S}} = \mathbf{0}$. The nature of these attractors is determined by the number of unstable eigenmodes for small fluctuations. If no eigenmodes are unstable, the fixed point is stable and is indicated by a filled circle. If one eigenmode is unstable, it is a hyperbolic fixed point (or equivalently a saddle node) and is marked as a cross. If two eigenmodes are unstable, it is an unstable fixed point and is represented by an open circle. For $\omega_0 \ll \kappa$ there are never more than two unstable eigenmodes, meaning that the state of the photon field rapidly comes to follow the state of the collective spin.

In order to gain some orientation we discuss the individual panels in Fig. 6. For the parameters used in Fig. 6(a), there is one stable attractor on the Bloch sphere corresponding to the normal state (⇓). This is the ultimate fate of the system for all initial conditions as indicated in Fig. 4; the inverted state (⇑) corresponds to an unstable fixed point. In passing to Fig. 6(b), the normal state (⇓) becomes an unstable hyperbolic fixed point and an SRA attractor with a nontrivial magnetization S_z (or its parity symmetry partner on the other side of the Bloch sphere) governs the long-time dynamics. In contrast, in Figs. 6(c), 6(d), and 6(e) we see multiple stable fixed points corresponding to the coexistence phases $\Downarrow + \Uparrow$, SRB$+ \Downarrow + \Uparrow$, and SRB$+ \Downarrow$, respectively; see Fig. 4. For these parameters, the final state of the system depends on the initial conditions, and we only highlight some typical trajectories. Nonetheless, the totality of stable fixed points completely accounts for the possible asymptotic behavior and therefore discriminates between different dynamical phases. In Fig. 6(f) we see both stable and unstable nontrivial fixed points

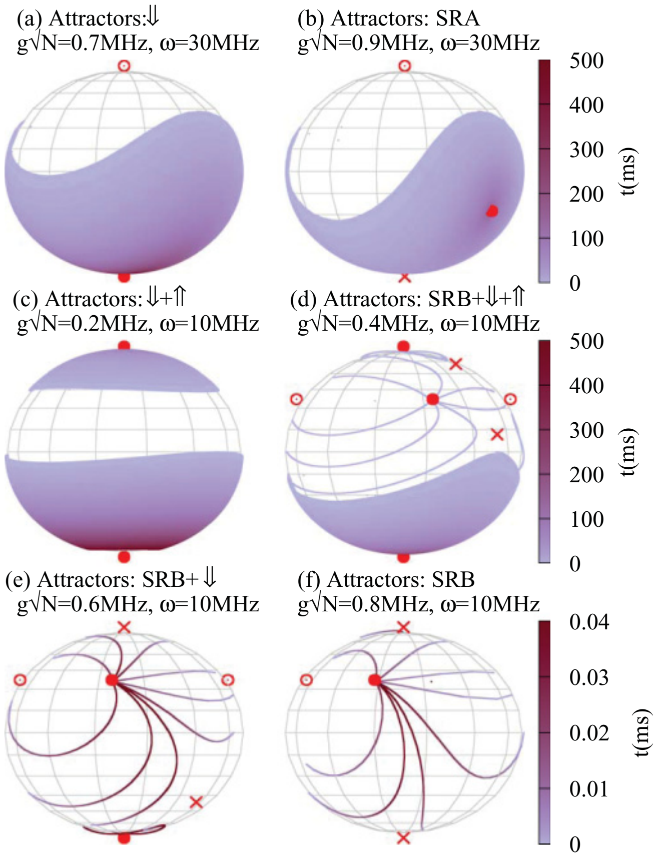

FIG. 6. (Color online) Bloch spheres with $|\mathbf{S}| = N/2$ corresponding to the points (a)–(f) in Fig. 4 showing the fixed points where $\dot{\mathbf{S}} = \mathbf{0}$ and $\dot{\psi} = 0$. We distinguish between stable fixed points (filled circles), unstable fixed points (open circles), and hyperbolic points with one stable and one unstable eigenmode (crosses). The presence of more than one stable attractor on the Bloch sphere corresponds to a coexistence phase in Fig. 4. The trajectories show the typical time evolution, where the initial conditions are chosen in order to illustrate the attractors. In particular, the time scale for approaching the SRA fixed point in (b) is significantly longer than the time scale for approaching the SRB fixed point in (f). In the language of dynamical systems the transition from (a) to (b) is a pitchfork bifurcation where a single mode goes unstable. The transition from (c) to (a) is a subcritical Hopf bifurcation where two modes go unstable simultaneously. The transition from (c) to (d) involves the appearance of eight additional fixed points; these correspond to two stable and two unstable SRB fixed points and four hyperbolic SRA fixed points. The transitions from (d) to (e) and (e) to (f) are inverse pitchfork bifurcations in which a pair of hyperbolic SRA fixed points coalesce at a previously stable fixed point.

---

[4] It is notable that in the regime where the dynamically stable phase is SRB, the equilibrium system considered in Ref. [62] for $\kappa = 0$ is thermodynamically unstable; the Hamiltonian is not bounded from below and the minimum-energy state occurs at infinite photon number. Such an infinite density is unphysical, particularly in the presence of a nonvanishing photon loss rate κ.

corresponding to the superradiant phase SRB; see Fig. 4. Note that in Fig. 6 we have focused on cases with $\omega > 0$. For $\omega < 0$ the fixed points can be immediately found from the duality under the transformation given in Eq. (5). This corresponds to inverting the Bloch spheres shown in Fig. 6.

While the attractors determine the long-time asymptotic behavior of the system, there are cases where the evolution proceeds on surprisingly long time scales. This may be seen in Figs. 6(a)–6(d), where the time scale for relaxation toward the fixed point is much longer than the period of the orbits encircling it; indeed, the latter cannot be resolved in these panels, leading to a dense covering of the Bloch sphere. In addition, the total time interval for approaching the SRA fixed point in Fig. 6(b) is much longer than that for approaching the SRB fixed point in Fig. 6(f). We will investigate this crucial distinction in more detail below.

C. Time evolution

In order to shed light on the dynamical distinction between the SRA and SRB fixed points, we examine the time evolution starting near the normal state ($\Downarrow$) for the parameters used in Figs. 6(b) and 6(f) with $\omega > 0$; see Fig. 7. By specifying an initial condition which is not a stable fixed point, the dynamical traces correspond to a sudden quench into the superradiant state. However, since the initial state corresponds to an unstable fixed point, the dynamics would remain stuck in the absence of noise or quantum fluctuations. In practice, these inherent fluctuations will destabilize the initial state, and a nontrivial time evolution will take place.

In order to probe the intrinsic quench dynamics we consider two different approaches for perturbing the initial condition. The first approach is to displace the initial state by $S_x = S_y = \sqrt{N}$, corresponding to the characteristic size of quantum fluctuations in the initial state; the subsequent semiclassical time evolution gives the pale gray trajectories in Fig. 7. The second approach is to use a Wigner-distributed ensemble of initial conditions in order to incorporate harmonic fluctuations around the normal state ($\Downarrow$); see for example Refs. [64,65] and Appendix F. The corresponding time dynamics is represented by the black lines in Fig. 7. It is readily seen that both the $\sqrt{N}$ displacement and Wigner approaches are in quantitative agreement regarding the overall time scales for evolution toward the SRA and SRB fixed points. Although the amplitude of the collective oscillations is partially washed out by the Wigner distribution of initial spin states, oscillations of the same period nonetheless remain in these examples.

Comparing the cases shown in Fig. 7, there is clearly a significant difference in the relaxation time scales. For evolution toward the SRA fixed point shown in the upper two panels of Fig. 7, there are oscillations at frequencies of a few kilohertz, with a decay time of order 100 ms. In contrast, for evolution toward the SRB fixed point shown in the bottom two panels of Fig. 7, the time scale of the "oscillation" is similar ($\sim$0.2 ms), but only one oscillation occurs before the steady state is reached. As discussed in Ref. [50], the remarkably slow dynamics near the SRA fixed point is related to the proximity to a dynamical phase boundary in the extended parameter space where g and g' are allowed to vary independently. We will return to explore this point further in Sec. VI B.

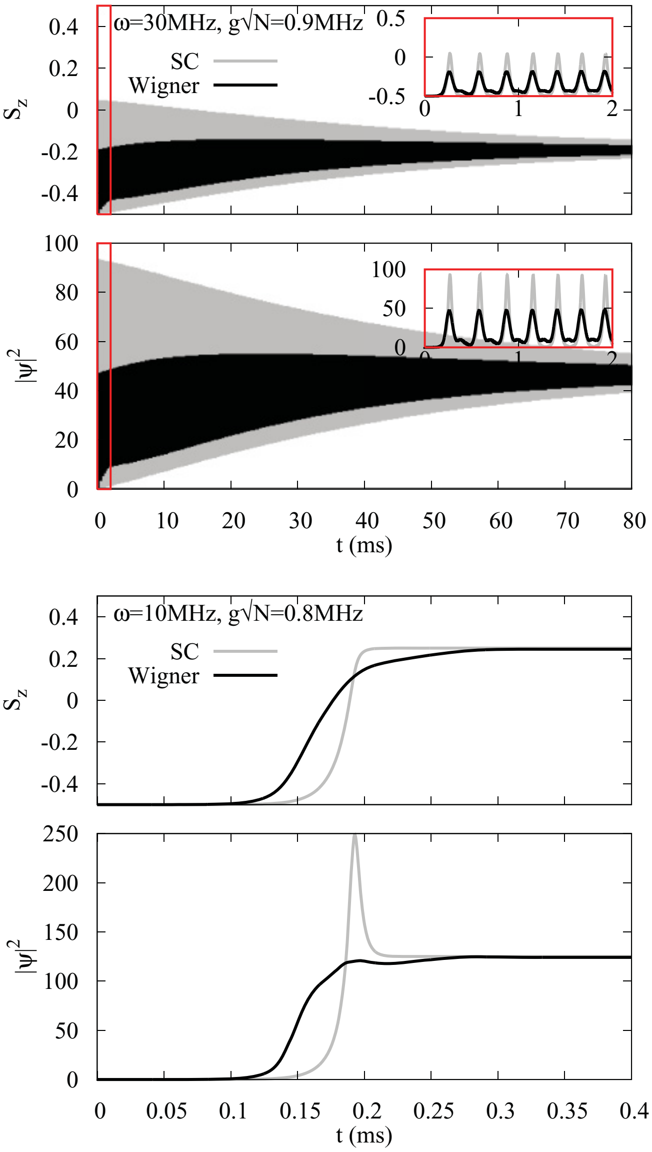

FIG. 7. (Color online) Time evolution in the superradiant regime with initial conditions that are close to the normal state ($\Downarrow$). The top two panels (and insets) correspond to point (b) in Figs. 4 and 6. The bottom two panels correspond to point (f). In each case, the evolution of the semiclassical equations for a single initial condition with $S_x = S_y = \sqrt{N}$ is shown in gray (marked SC). The average evolution for a Wigner-distributed ensemble of initial conditions is shown in black. The insets in the top two panels show magnified images of the highlighted regions.

Thus far we have considered the time evolution at points (b) and (f) in Fig. 4, corresponding to $\omega > 0$. For completeness we should also consider the time evolution at point (g) with $\omega < 0$. Owing to the duality in Eq. (5), the dynamics starting from $S_z = -N/2$ with $\omega > 0$ is related to the dynamics starting from $S_z = N/2$ with $\omega < 0$. We should therefore consider the quench dynamics starting from $S_z = -N/2$ and $\omega < 0$ separately. This is illustrated in Fig. 8, along with the accompanying dynamics on the Bloch sphere. It is notable that the dynamics in this regime where $\omega_- < 0$ has a remarkably long time scale. From the Bloch sphere, and the time dependence of S_z, it is clear where this comes from: the trajectory first spirals around

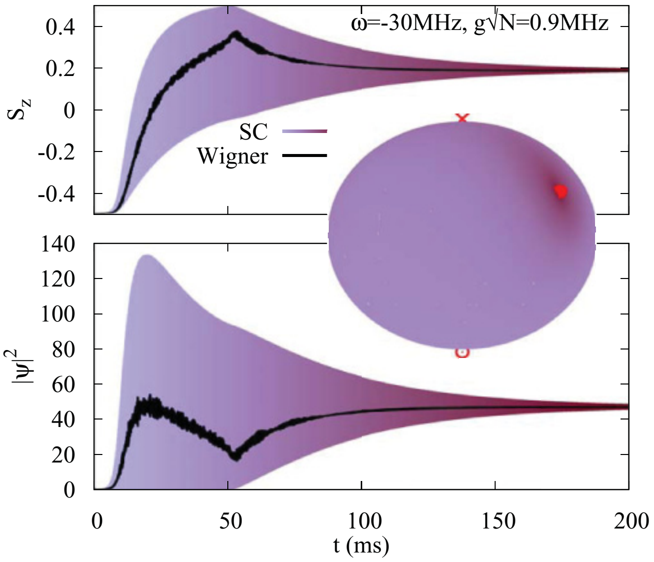

FIG. 8. (Color online) Time evolution starting close to the normal state (⇓) for the parameters at point (g) in Fig. 4. As in Fig. 7, the semiclassical dynamics for both a single starting point with $S_x = S_y = \sqrt{N}$ (marked SC) and a Wigner-distributed set of initial conditions are shown. The latter is indicated in black, and the semiclassical trajectory is shaded to match the Bloch sphere shown as an inset; for these initial conditions the trajectory almost covers the Bloch sphere.

the unstable normal state (⇓), growing in amplitude, until it reaches the stable manifold of the hyperbolic inverted state (⇑), from which it then transfers to spiral around the stable attractor. As such, almost the entire Bloch sphere is covered by this trajectory, and a very long waiting time of order 0.2 s is required before reaching the asymptotic state. In contrast to Fig. 7 the long-time asymptote is not reached after 100 ms. In Sec. V we will consider the implications of this type of behavior for the phase diagram obtained in the experiments of Ref. [22], which have a finite duration of order 10 ms.

V. GROWTH AND DECAY TIMES AND IMPLICATIONS FOR FINITE-DURATION EXPERIMENTS

In the above discussion, we have seen that the time scale for reaching the asymptotic attractors varies considerably between different points in parameter space. In order to make contact with experiment [22], it is therefore crucial to understand how this time scale varies throughout the phase diagram. In this section we address this key issue.

It is evident from Fig. 8 that in order to characterize the temporal evolution we require at least two principal time scales. The first is the time scale for departing from the initial state, and the second is the time scale for approaching the final asymptotic attractor. Both of these time scales may be extracted by linearizing around the initial and final states as appropriate, and calculating the eigenvalues (frequencies) using the methods outlined in Sec. III C and Appendix C. In Fig. 9 we use these eigenvalues to plot the characteristic time for the normal state to become unstable, if it does so, and the characteristic decay time in the approach toward the final state; in the case of asymptotic coexistence phases we focus on the state that is actually reached in a quench experiment that starts close to the normal state (⇓). It is clear from Fig. 9 that both of these fundamental time scales vary significantly throughout the phase diagram. In particular, in the region where $\omega_- < 0$, both the time scale for the initial destabilization of the normal state and the time scale for decay toward the asymptotic state are increased. The combination of these two time scales provides a lower bound on the overall duration of the intrinsic dynamics. For $\omega_- < 0$ we therefore expect a slower approach to the asymptotic regime. In order to gain a better handle on this issue, we provide an analytic discussion of the constituent time scales below. We begin in Sec. V A 1 with an analysis of the initial growth times before examining the final asymptotic decay times in Sec. V A 2. In Sec. V B we then consider the implications for experiments which monitor the photon intensity over a finite time interval.

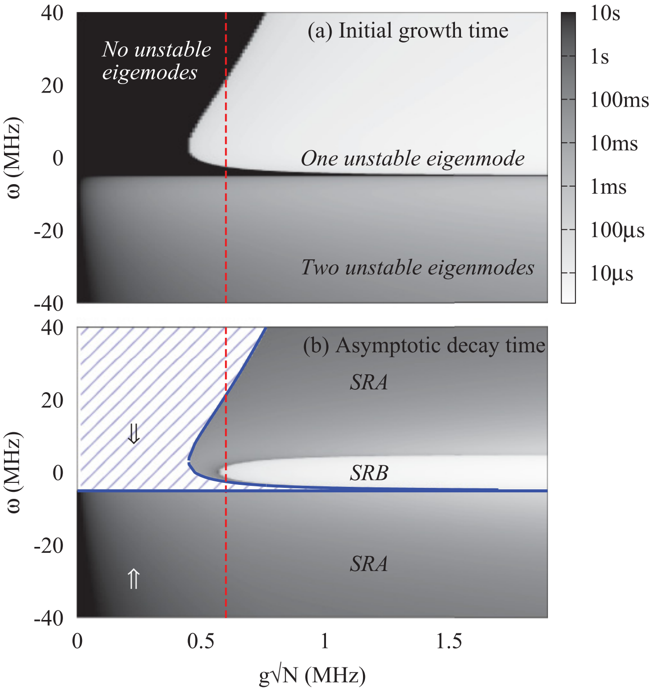

FIG. 9. (Color online) Characteristic time scales of the semiclassical dynamics. We use the same parameters as in Fig. 4 with $UN = -10$ MHz corresponding to the experiments of Ref. [22]. (a) shows the time required for the instability of the initial ground state (⇓) to develop; in regions where this state is stable this time scale is taken to ∞. (b) shows the asymptotic time scale for approaching the final stable state. In the regions of multistability, the rate of attraction to the final state for the given initial conditions (⇓) is shown. In both panels the time scales show a strong variation throughout the phase diagram, with notable implications for finite-duration experiments. A vertical slice along the red dashed line is given in Fig. 10.

A. Growth and decay times

1. *Growth times*

The initial growth time in Fig. 9(a) can be understood and estimated analytically, by using the linearization discussed in Sec. III C. Considering Eq. (15) for the normal state with $S_z = -N/2$ the eigenvalues η obey

$$[(\eta + i\kappa)^2 - \omega_-^2](\eta^2 - \omega_0^2) - 4\omega_0\omega_- g^2 N = 0, \qquad (16)$$

where $\omega_- \equiv \omega - UN/2$. To obtain the growth rate for a given set of parameters we must find the solution of Eq. (16) with the largest positive imaginary part η''. Solving Eq. (16) numerically, we plot the corresponding growth time $1/\eta''$ in Fig. 9(a). It is evident that there are distinct growth times in the top and bottom portions of Fig. 9(a) separated by the critical line $\omega_- = 0$. The origin of this distinction may be traced to a change in behavior of the root structure of Eq. (16). For the parameters shown in Fig. 9(a), when $\omega_- > 0$ a single one of the four roots goes unstable, while for $\omega_- < 0$ two roots with same imaginary parts go unstable simultaneously. In the language of dynamical systems, the first scenario corresponds to a pitchfork bifurcation, whilst the latter corresponds to a Hopf bifurcation [66].

In order to gain a quantitative handle on the observed growth times, we may exploit the small parameter ω_0/κ in order to find analytic approximations for η. Anticipating that $|\eta| \sim \omega_0 \ll \kappa$ we neglect η in the combination $\eta + i\kappa$. This yields a quadratic equation which provides

$$\eta \approx \pm\sqrt{\omega_0^2 - \frac{4\omega_0\omega_- g^2 N}{\omega_-^2 + \kappa^2}} = \pm\omega_0\sqrt{1 - \left(\frac{g}{g_a^-}\right)^2}, \tag{17}$$

where g_a^- is given in Eq. (11) and the plus sign corresponds to the growing mode. For $g > g_a^-$, η is imaginary, and the characteristic growth rate is indeed of order ω_0 as we assumed. However, for $\omega_- < 0$ it is evident from the first form of Eq. (17) that $\eta \in \mathbb{R}$ and therefore Eq. (17) cannot apply in the lower region of Fig. 9(a). To fully describe the observed behavior it is necessary to carry out the expansion of η to higher order in ω_0/κ. Parametrizing $\eta = \pm\omega_0\sqrt{1 - (g/g_a^-)^2} + \delta_\pm$, where $\delta_\pm \ll \omega_0 \ll \kappa$, and substituting into Eq. (16), one obtains

$$\eta \approx \pm\omega_0\sqrt{1 - \left(\frac{g}{g_a^-}\right)^2} - \frac{4i\kappa\omega_0\omega_- g^2 N}{(\omega_-^2 + \kappa^2)^2}. \tag{18}$$

As shown in Fig. 10(a), the root with the plus sign in Eq. (18) accurately reproduces the exact growth times observed in Fig. 9(a). In particular, for $\omega_- > 0$ one may neglect the last term in Eq. (18), but for $\omega_- < 0$ it is essential to retain this contribution as the leading term no longer corresponds to a decay rate. In the former case where $\omega_- > 0$, the decay rate is typically of order $\omega_0 = 0.05$ MHz; this corresponds to a time scale of 20 μs, in agreement with the upper region of Fig. 9(a) and the central portion of Fig. 10(a). In the latter case, where $\omega_- < 0$, the decay rate is of order $\omega_0^2/\kappa \simeq 0.3$ kHz, where we use the functional dependence of the critical coupling in Eq. (11). This corresponds to a much longer time scale of order 3 ms, in agreement with the lower region of Fig. 9(a) and the left-hand side of Fig. 10(a). In fact the exact time scales diverge on approaching the phase boundaries where the $\Downarrow$ state is stable; see Fig. 10(a). This may also be interpreted as critical slowing down [50]. For example, approaching the left region of $\Downarrow$ in Fig. 10(a) from the right, one has $\eta \sim \sqrt{g_a^- - g}$; this is analogous to an equilibrium mean-field exponent $z\nu = 1/2$. On the other hand, approaching the left region of $\Downarrow$ from the left, one has $\eta \sim (\omega - UN/2)$. This latter behavior arises from the second term in Eq. (18) and exists only in the open system with $\kappa \neq 0$; it is analogous to a critical exponent $z\nu = 1$. A divergent growth time may also be seen in the lower left corner of Fig. 9(a), since $g \to 0$ in the second term of Eq. (18). For recent discussions of critical behavior in driven open cavities, see Refs. [67–70].

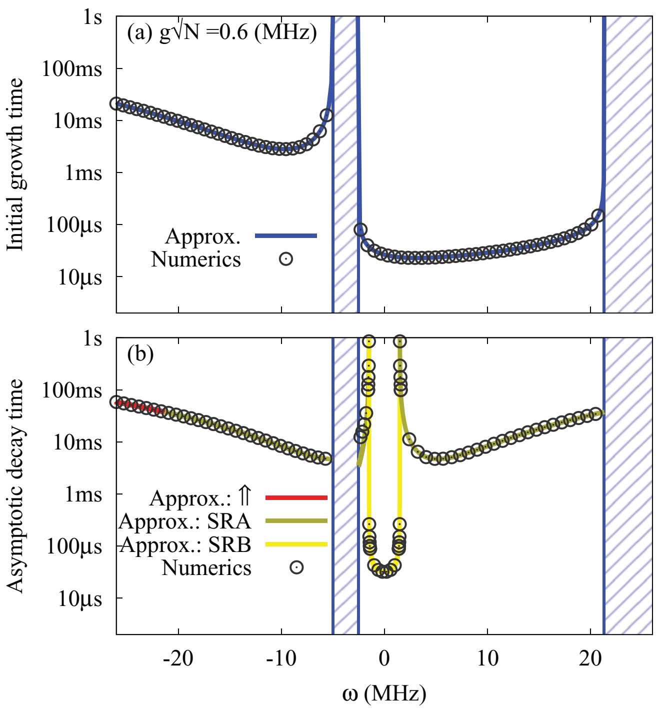

FIG. 10. (Color online) Vertical slice through Fig. 9 with $g\sqrt{N} = 0.6$ MHz. (a) Initial growth time obtained by linear stability analysis around the normal ($\Downarrow$) state. The open circles show the exact semiclassical results obtained numerically from the quartic Eq. (16). The solid line corresponds to the approximation given in Eq. (18) where the plus sign corresponds to the unstable mode. (b) Asymptotic decay time obtained by linear stability analysis around the appropriate final asymptotic state. The open circles correspond to the eigenvalue of $|\eta\tilde{\mathbb{I}} - \tilde{\mathbb{M}}| = 0$ with the largest imaginary part, where $\tilde{\mathbb{M}}$ is given by Eq. (C5). The solid gold (mid gray) line corresponds to the imaginary part of Eq. (20) and the solid yellow (light gray) line corresponds to the exact result in Eq. (22). In both panels, the shaded regions indicate where the normal state ($\Downarrow$) is stable. Both time scales show a strong dependence on the parameters.

2. *Decay times*

Turning to the asymptotic decay time in Fig. 9(b), we consider the approach toward the three stable fixed points $\Uparrow$, SRA, and SRB, which differ from the initial state $\Downarrow$. In order to extract the associated time scales we must linearize around the asymptotic fixed points and find the eigenvalue with the smallest imaginary part.

For decay toward the inverted state ($\Uparrow$), we may invoke our previous result in Eq. (18) with the replacement $\omega_- \to \omega_+$. In order to extract the time scale governing the approach toward the SRA state, we must linearize around this fixed point. Following the general approach used in Sec. III C, this yields the characteristic equation

$$[(\eta + i\kappa)^2 - \tilde{\omega}^2]\left[\eta^2 - \left(\frac{\tilde{\omega}_0 N}{2S_z}\right)^2\right] = -\frac{2\tilde{\omega}_0\tilde{\omega}}{S_z}|2gS_z - U\psi S_x|^2, \tag{19}$$

where $\tilde{\omega} \equiv \omega + US_z$ and $\tilde{\omega}_0 \equiv \omega_0 + U|\psi|^2$ are useful variables suggested by Eq. (3); for more details see Appendix C and Eq. (C11). The ultimate time scale controlling the decay toward the fixed point is governed by the slowest roots of Eq. (19). Anticipating that these have $|\eta| \sim \tilde{\omega}_0 N/2S_z \ll \kappa$, we may once again neglect the term η in the combination $\eta + i\kappa$. This yields a quadratic equation for η with solutions $\eta = \pm\eta_0$ where $\eta_0 \in \mathbb{R}$. In order to refine this approximation, we parametrize $\eta = \pm\eta_0 + \delta_\pm$ where $\delta_\pm \ll \omega_0 \ll \kappa$, and substitute into Eq. (19). Retaining terms up to linear order in δ, one obtains

$$\eta \approx \pm\eta_0 + \frac{2i\kappa\tilde{\omega}_0\tilde{\omega}|2gS_z - US_x\psi|^2}{(\tilde{\omega}^2 + \kappa^2)^2 S_z}. \tag{20}$$

In the limit $U = 0$ one finds $\mathrm{Im}(\eta) \approx -\kappa\omega_0^2/(\omega^2 + \kappa^2)$, where we use Eq. (9) to substitute for S_z. This agrees with our previous findings [50] and yields a characteristic decay rate of order $\omega_0^2/\kappa \simeq 0.3$ kHz. This is consistent with the 3 ms time scale found in Figs. 9(b) and 10(b). In addition, in the limiting case of the SRA phase where $\psi = 0$ and $S_z = -N/2$, we recover the characteristic frequencies of the normal ($\Downarrow$) state as given by Eq. (18). As shown in Fig. 10(b), Eq. (20) accurately reproduces the results obtained by direct numerical solution of Eq. (19).

For decay toward the SRB state, the results are much simpler. In this case the characteristic frequencies satisfy

$$[\eta(\eta + i\kappa) - 4gU\psi_2 S_y]^2 = 0, \tag{21}$$

where $\psi \equiv \psi_1 + i\psi_2$; see Appendix C. In the case of the stable SRB fixed points discussed in Sec. III B 2, where $(\psi, S_y) = \pm(i\sqrt{(-\omega_0/U)}, |S_y|)$, one readily obtains exact results for the repeated roots of Eq. (21):

$$\eta = -i\frac{\kappa}{2} \pm \sqrt{-\frac{\kappa^2}{4} + 2\omega_0\kappa\sqrt{\frac{g^2 - g_b^2}{g_b^2}}}, \tag{22}$$

where we use the fact that $S_y^2 = \omega_0\kappa^2(g^{-2} - g_b^{-2})/4U$. The decay toward the SRB state is governed by the slowest mode corresponding to the positive root in Eq. (22). Since $\omega_0 \ll \kappa$ we may Taylor-expand this root to obtain $\mathrm{Im}(\eta) \simeq -2\omega_0\sqrt{g^2/g_b^2 - 1} + O(\omega_0^2/\kappa)$. As shown in Fig. 10(b), the exact analytical result (22) is in agreement with the numerical solution of Eq. (21) as required.

From the above analysis we see that the characteristic decay rates toward the SRA and SRB states are of order ω_0^2/κ and ω_0, respectively. These correspond to decay times of the order of 3 ms and 20 μs, which yields a faster approach toward the SRB phase in comparison to the SRA phase. This is confirmed by the typical trajectories on the Bloch sphere as shown in Figs. 6(b) and 6(f). It is readily seen that many more orbits are executed in reaching the SRA fixed point. We see that the SRA and SRB attractors differ in their dynamic characteristics, in addition to their steady-state forms.

B. Photon intensity map extracted at intermediate times and implications for finite-duration experiments

Having examined the characteristic growth and decay times across the phase diagram, we now consider the consequences for finite-duration experiments. In particular, for $\omega_- < 0$, the semiclassical dynamics predicts relatively long growth times and comparably long approach times, as shown in Fig. 9. In Fig. 11 we compare the resulting photon intensity map obtained after a hypothetical infinite-duration experiment to that obtained after 10 ms. It is readily seen that the lower region, corresponding to $\omega_- < 0$, has not fully reached the asymptotic regime.

In order to make close contact with the experiment of Ref. [22], we should also incorporate the details of their data aquisition scheme. In particular, the photon intensity map is obtained by increasing the laser intensity over a 10 ms interval and recording the photon intensity during this period. This procedure is then repeated for other detunings and an intensity map is generated. In order to facilitate a direct comparison, we incorporate the effects of the sweep in our numerical simulations, where we take $g^2 \propto t$. In Fig. 12(a) we

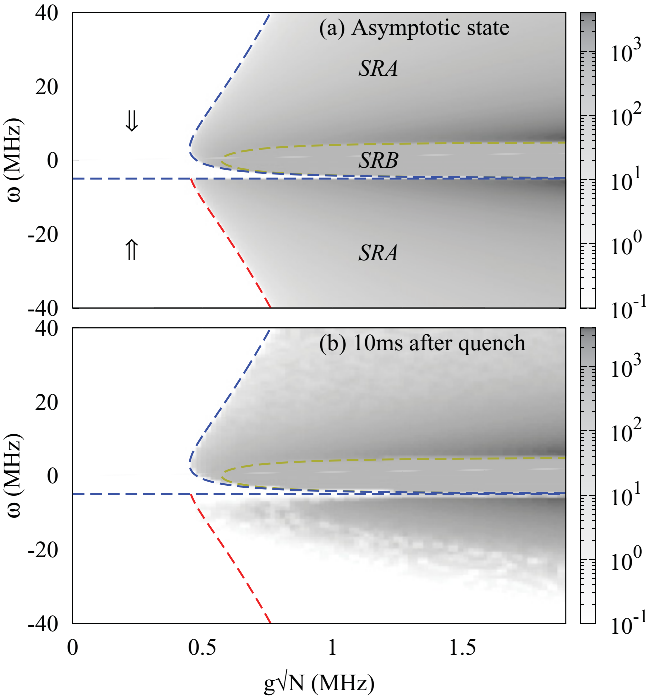

FIG. 11. (Color online) Photon intensity maps showing $|\psi|^2$ after two different time intervals, with initial conditions that are close to the normal state ($\Downarrow$) with $S_x = S_y = \sqrt{N}$. We use the same parameters as in the second panel of Fig. 4 with $UN = -10$ MHz, corresponding to the experiments of Ref. [22]. (a) Intensity map obtained in the final asymptotic state with $t \to \infty$, showing the distinct regions of SRA, SRB, and $\Uparrow$ states. (b) Intensity map obtained after 10 ms showing good qualitative agreement with the asymptotic attractors in (a), but with a slower approach in the SRA regions. A cross section of (a) with $g\sqrt{N} = 1.0$ MHz is provided in Fig. 5.

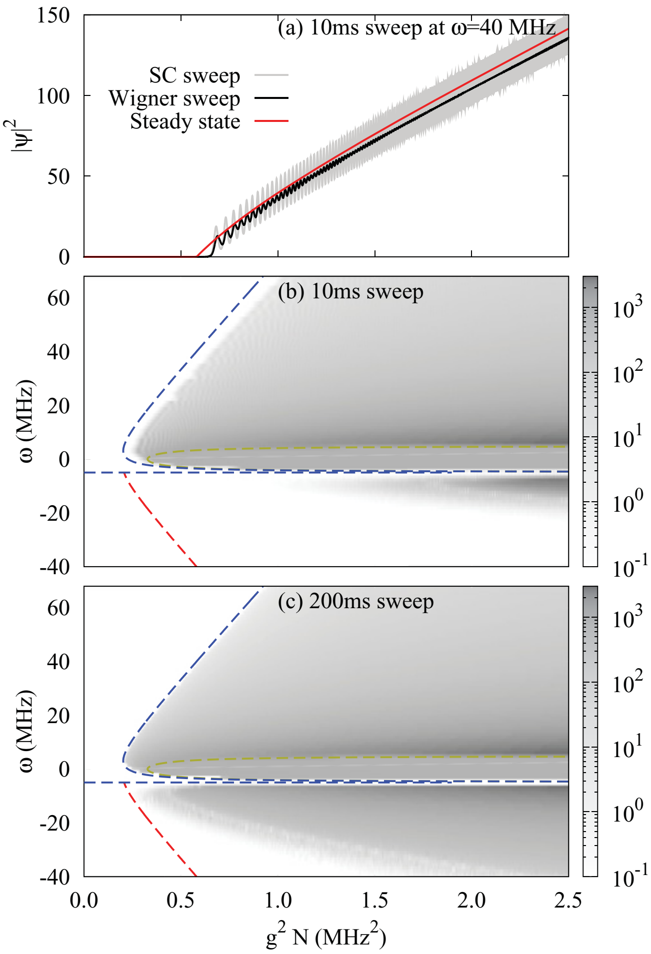

FIG. 12. (Color online) $|\psi|^2$ found by increasing $g^2 \propto t$ and recording the value achieved as a function of time. We use the same parameters as in Fig. 4 with $UN = -10$ MHz, corresponding to the experiments of Ref. [22]. The sweep is chosen so that $g^2N = (t/t_0) \times 2.5$ MHz^2, where $t_0 = 10$ ms in (a) and (b) and $t_0 = 200$ ms in (c). The top two panels correspond to the experimental sweep duration used in Ref. [22]. (a) Comparison of the steady-state value of $|\psi|^2$ with that obtained by a semiclassical evolution (marked SC) and Wigner-distributed initial conditions, for the value of $g\sqrt{N}$ reached at a given time with $\omega = 40$ MHz. (b) Photon intensity map obtained after a 10 ms sweep. (c) Photon intensity map obtained after a 200 ms sweep. In comparing these figures to Fig. 5 of Ref. [22], one should note that the vertical scale on our intensity plots is the photon frequency ω appearing in Eq. (2). In comparison, the authors of Ref. [22] use the detuning of the pump from the bare-cavity frequency as the vertical scale, hence the inverted and shifted axis.

show how, for one value of ω, $|\psi|^2$ evolves with increasing matter-light coupling. We take $g^2N = (t/t_0) \times 2.5$ MHz^2, where $t_0 = 10$ ms in Figs. 12(a) and 12(b), and 200 ms in Fig. 12(c). As discussed in Sec. IV C, we present both a single semiclassical trajectory with $S_x = S_y = \sqrt{N}$ and the results of Wigner-distributed initial conditions. As found previously, it is readily seen from Fig. 12(a) that quantum fluctuations reduce the oscillations in the photon intensity, but that the overall dependence conforms to the semiclassical analysis. Moreover, for this set of parameters, the results of the 10 ms sweep are also in good agreement with the steady-state photon intensity. We may therefore use the semiclassical approach to map out the resultant phase diagram.

A notable finding is that, in other regions of the phase diagram, sweeps longer than 10 ms may be required in order to reveal signatures of the asymptotic attractors. To see this more clearly, in Figs. 12(b) and 12(c) we show the results of the semiclassical evolution in Eq. (3), with $\sqrt{N}$ displacement of the initial state, and a sweep profile. It is readily seen that for $\omega_- > 0$ the results of the 10 ms sweep are already quite close to those for the long-time asymptotic state. However, as can be anticipated by the large instability growth and asymptotic approach times for $\omega_- < 0$, the normal state ($\Downarrow$) persists. Despite its ultimate instability, the 10 ms is insufficient for the instability to grow. In contrast, with a sweep duration of 200 ms, one can see the instability of the normal state in this region, although the final asymptotic state of the semiclassical dynamics has not been reached.

VI. GENERAL PHASE DIAGRAM

Having discussed the phase diagram and the collective dynamics for the experimentally explored case with $g = g'$ and $U < 0$ [22], we now consider the broader parameter space. In Sec. VI A we consider the case with $g = g'$ and $U > 0$, and in Sec. VI B we examine the case with $g \neq g'$. Notable features of both of these cases are parameter regimes in which no stable fixed point exists and for which persistent oscillations arise.

A. Phase diagram for $g = g'$ and $U > 0$

The sign of U can be varied by switching between red and blue detuning of the cavity light field with respect to the atomic transition. This may be seen from the derivation of the effective Dicke model Hamiltonian, as outlined in Sec. II and Appendix A. In Fig. 13 we show the resulting phase diagram with $g = g'$ and $U > 0$; this is the analog of the phase diagram shown in Fig. 4.

With $U > 0$, the phase boundaries at $\omega_\pm = 0$ shift in the opposite direction to those obtained with $U < 0$. As such, the boundaries separate, rather than overlap, as shown in Fig. 13. Instead of finding coexistence phases, as found in Fig. 4, a regime of persistent oscillations emerges as shown in white in Fig. 13. In this region, no steady state is ever reached, and the photon number continues to oscillate periodically at long times. This is illustrated in Fig. 14.

For these persistent oscillations with $g = g'$ it is possible to characterize their behavior analytically. In this case the emergent state is a limit cycle [50]. To see this one may note from Fig. 14 that the asymptotic behavior has constant S_z, and in fact $S_z = -\omega/U$. From the equations of motion in Eq. (3), we see that $\dot{S}_z = -ig(\psi + \psi^*)(S^+ - S^-)$. However, it also clear from Fig. 14 that $S_y \neq 0$ and so $S^+ \neq S^-$. We therefore require Re$(\psi) = 0$, as found in the SRB steady state. With these conditions on S_z and ψ, Eq. (3) simplifies. Writing $S^- = re^{-i\theta}$, where $r^2 = N^2/4 - \omega^2/U^2$ is a constant of the motion, one obtains

$$\dot{\theta} = \omega_0 + U|\psi|^2, \quad \dot{\psi} + \kappa\psi = -2igr\cos\theta. \tag{23}$$

This pair of coupled first-order equations describes the exact dynamics of the persistent oscillations. Since the motion is

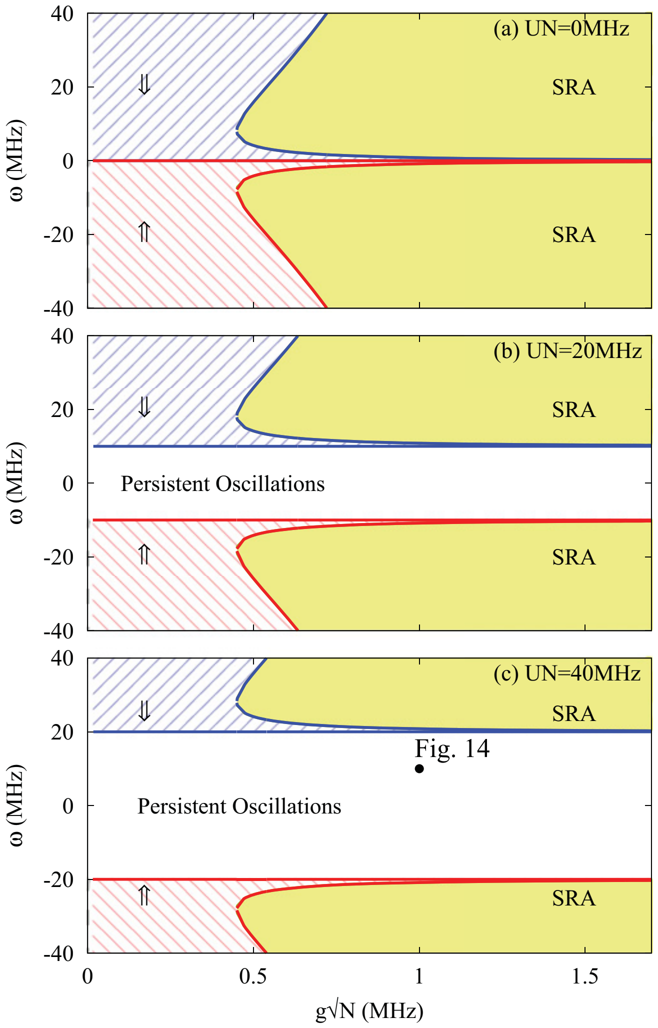

FIG. 13. (Color online) Dynamical phase diagram as a function of ω and $g = g'$ for $U \geqslant 0$. The phase boundaries at $\omega_{\pm} = 0$ separate with increasing U, and a regime of persistent oscillations emerges. The dynamics in this regime is shown in Fig. 14. In contrast to Fig. 4, the SRB phase is absent here since $U \geqslant 0$.

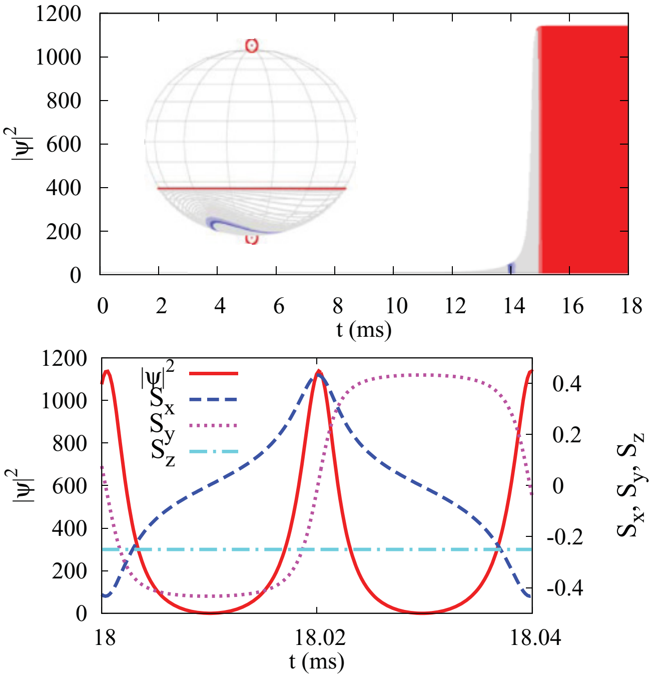

FIG. 14. (Color online) Persistent oscillations at $\omega = 10$ MHz, $UN = +40$ MHz, and $g\sqrt{N} = 1$ MHz, starting close to the normal state ($\Downarrow$) with $S_x = S_y = \sqrt{N}$. The upper panel shows the attraction toward persistent oscillations, illustrating the transient behavior at short times and the persistent oscillations at later times. The inset shows the same data on the Bloch sphere using the same shading scheme. For all times after ~15 ms, the trajectory on the Bloch sphere is restricted to a circle at constant polar angle. The lower panel shows the time dependence of $|\psi|^2$ and $\mathbf{S}$ in the persistent-oscillation regime.

in a two-dimensional plane, the attractor is a simple limit cycle [66]. In Eq. (23), the phase angle θ continually increases, but has alternate fast and slow regions; the motion is faster when $|\psi|$ is larger as may be seen in Fig. 14. Such behavior is analogous to that of a damped driven pendulum. In fact, for $\kappa \gg \omega_0 + U|\psi|^2$, one may adiabatically eliminate $|\psi|$ to obtain $\dot{\theta} = (\omega_0 + \lambda) + \lambda\cos(2\theta)$ where $\lambda = Ug^2r^2/2\kappa$. This is the equation of motion for a damped driven pendulum, and since $\omega_0 > 0$ it is driven above the threshold required for persistent oscillations.

B. Phase diagram for $g \neq g'$

Up until now, we have mainly restricted our discussion to the experimentally realized case where one necessarily has $g = g'$ [22]. However, there are important reasons to explore what happens when this condition is relaxed. In particular, there are a number of phase boundaries in the extended g,g' parameter space, and these can be rather close to the experimental situation with $g = g'$. As highlighted in Ref. [50], proximity to these phase boundaries is instrumental in explaining regions of slow decay in the $g = g'$ dynamics. Second, the proposal of Dimer *et al.* [34] considers a Raman scheme, rather than Rayleigh scattering, and involves different hyperfine atomic states. In this setting, separate tuning of g and g' could be achieved by using circularly polarized pump beams in a ring cavity [34]. For these reasons, we consider the behavior for $g \neq g'$.

In Fig. 15 we set $UN = -40$ MHz and explore deformations by $\delta g \equiv g' - g$ at four different values of fixed $\bar{g} \equiv \frac{1}{2}(g + g')$. There are three key aspects to note. The first concerns the existence of nontrivial phase boundaries in proximity to the $\delta g = 0$ or $g = g'$ axis. In particular, as one transits along the $\delta g = 0$ axis in Fig. 15(d), there are two distinct scenarios depending on whether $|\omega| > |\omega_u|$ or $|\omega| < |\omega_u|$, where $\omega_u \equiv UN/2$. In the former case there is a proximate phase boundary for small $\delta g/\bar{g}$ and associated critical slowing down. In the latter case the closest phase boundary is horizontal and is therefore not crossed by changing δg. Therefore, for a broad range of $|\omega| < |\omega_u|$, one may avoid close proximity to a phase boundary and the associated critical slowing down. This ω dependence of the emergent time scales is confirmed in Fig. 7. The second notable feature in Fig. 15(d) is that the SRA and SRB phases, which are distinct for $g = g'$, are continuously connected for $g \neq g'$. This may be traced

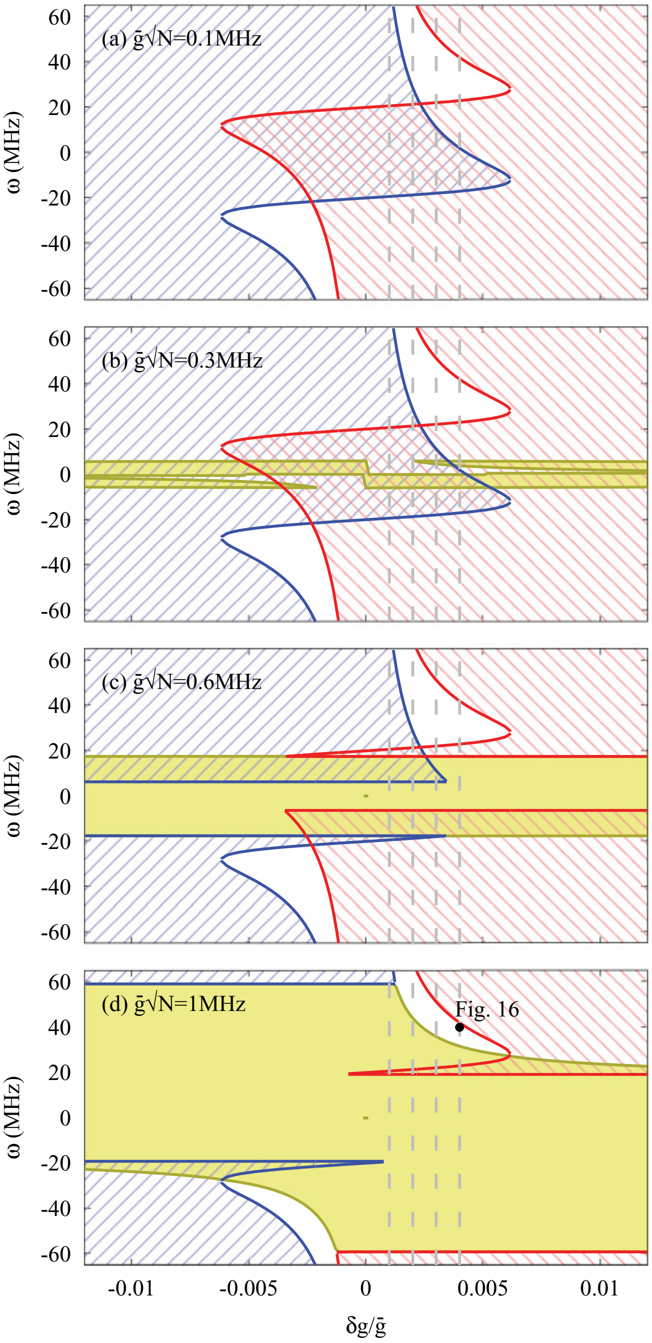

FIG. 15. (Color online) Dynamical phase diagram at $UN = -40$ MHz as a function of $\delta g \equiv g' - g$ and ω for a number of values of $\bar{g} = \frac{1}{2}(g + g')$. Vertical dashed lines indicate cuts shown in Fig. 18.

to the lack of factorization of the equation of motion for $\dot{S}_z$, which simplifies at $g = g'$ to $\dot{S}_z = -ig(\psi + \psi^*)(S^+ - S^-)$. The third notable feature is that there are again regions of persistent oscillations, shown in white, where no stable fixed points exist. As shown in Fig. 16, the detailed dynamics differs from the persistent oscillations discussed in Sec. VI A, as may be seen from the feature that S_z is no longer constant.

In general it may be difficult to gain a purely analytic handle on the equations of motion in Eq. (3) when $g \neq g'$ and U is present. However, in the adiabatic limit with $\kappa \to \infty$ one may

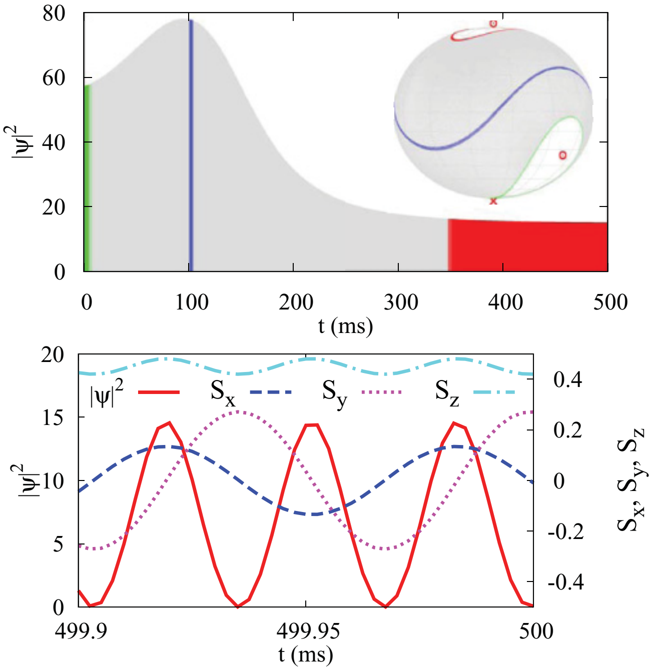

FIG. 16. (Color online) Persistent oscillations for $UN = -40$ MHz, $\omega = 40$ MHz, $g\sqrt{N} = 0.998$ MHz, and $g'\sqrt{N} = 1.002$ MHz, corresponding to $\delta g/\bar{g} = 0.004$ or $g'/g = 1.004$. The panels mirror those in Fig. 14. The shading in the top panel match those in the inset, highlighting the initial and intermediate trajectories, and the final persistent oscillations.

eliminate the photons and consider the dynamics of the spins alone. In this limit the equations of motion reduce to the form

$$\dot{\mathbf{S}} = \{\mathbf{S}, H\} - \mathbf{D}_1(\mathbf{S}) - \mathbf{D}_2(\mathbf{S}), \tag{24}$$

where the effective Hamiltonian is given by

$$H = \omega_0 S_z - \frac{\tilde{\omega}\left(G_+ S_x^2 + G_- S_y^2\right)}{\kappa^2 + \tilde{\omega}^2}, \tag{25}$$

with $\tilde{\omega} \equiv \omega + U S_z$. The additional contributions

$$\begin{aligned} \mathbf{D}_1 &= \frac{2\kappa\Gamma \mathbf{S} \times (\mathbf{S} \times \hat{\mathbf{z}})}{\kappa^2 + \tilde{\omega}^2}, \\ \mathbf{D}_2 &= \frac{2\kappa^2 U\left(G_+ S_x^2 + G_- S_y^2\right)}{(\kappa^2 + \tilde{\omega}^2)^2} \mathbf{S} \times \hat{\mathbf{z}} \end{aligned} \tag{26}$$

are damping terms with $G_\pm \equiv (g' \pm g)^2$ and $\Gamma \equiv g'^2 - g^2$. The existence of the photon leakage κ therefore means that there are two non-Hamiltonian terms in the effective spin dynamics. In the special case where $U = 0$ the term $\mathbf{D}_1$ has the same form as the damping in the Landau-Lifshitz-Gilbert equations [71,72] and $\mathbf{D}_2 = \mathbf{0}$. The former tries to drive the system toward either the normal or the inverted state. In this $U = 0$ limit the Hamiltonian contribution in Eq. (25) also reduces to an effective Lipkin-Meshkov-Glick Hamiltonian [73–76].

A notable aspect of the adiabatic limit with $\kappa \to \infty$ is that the resulting dynamics in Eq. (24) resides solely within the two-dimensional surface of the Bloch sphere. The Poincaré-Bendixson theorem [66] therefore excludes the possibility of chaotic attractors. In contrast, for $\kappa = 0$, the conservative

Dicke model with $g = g'$ and $U = 0$ is known to exhibit chaotic behavior in the superradiant regime [31,32]. In view of this difference, it would be interesting to explore the possibility of strange attractors for intermediate κ. However, for the parameters we have explored numerically we see no evidence for strange attractors. Indeed, for $g = g'$ and $U > 0$ we have demonstrated the existence of a limit cycle governed by Eq. (23). Nonetheless, it is worth noting that the nonlinear equations of motion in Eq. (3) are closely related to the Maxwell-Bloch equations for a laser [77]. These are known to be equivalent to the paradigmatic Lorenz equations [78], the archetypal example of dissipative chaos. However, an important difference from the Maxwell-Bloch equations is the absence of external driving in Eq. (3). It would be instructive to explore the ramifications of this in more detail. For work on chaos in a closely related optomechanical system, see Ref. [79]. Further discussion of the phase diagram for $g \neq g'$ is given in Appendix E.

VII. BEYOND THE EFFECTIVE DICKE MODEL AND ITS SEMICLASSICAL TREATMENT

In the preceding sections, we have discussed the semiclassical dynamics of the nonequilibrium Dicke model and its relation to experiments on the self-organization of BECs in optical cavities [22]. Within the semiclassical description of this model, we have found a rich variety of stable attractors including nontrivial steady states, persistent oscillations, and regimes of bistability. Having established a wide variety of predictions for the semiclassical behavior of the open Dicke model, we now consider what effects may arise in going beyond this effective description. In Sec. VII A we first consider modifications to the Dicke model itself, arising from higher-momentum states and other terms in the effective Hamiltonian. In Sec. VII B we briefly comment on the possible modifications due to higher-order quantum effects.

A. Modifications of the effective Dicke model

As outlined in Sec. II, the derivation of the effective Dicke model involves a projection onto the subspace of the two lowest-lying momentum states; see Appendix A. Without this projection, there would also exist coupling to higher-momentum states such as

$$\frac{1}{\sqrt{2}}\sum_{\alpha=\pm}|\alpha 2k,0\rangle, \quad \frac{1}{\sqrt{2}}\sum_{\alpha=\pm}|0,\alpha 2k\rangle, \quad \frac{1}{2}\sum_{\alpha\beta=\pm}|\alpha 2k,\beta 2k\rangle. \tag{27}$$

In general, the occupation of these excited states is expected to be small for low-intensity cavity light fields, as supported by the time-of-flight images of Ref. [22]. Nonetheless, there are regimes of parameter space where these states may be important. In particular, these high-momentum states may destabilize certain phases predicted by the reduced Dicke model. Specifically, the inverted state involves excitation to the north pole of the Bloch sphere and may be susceptible to destabilization. Indeed, in the parameter regimes where the effective Dicke model predicts the inverted state, kinetic approaches predict heating [80]. Likewise, regions of the superradiant phase in which the majority of the atoms are in the nonzero-momentum state may be unstable.

Although the stability of these particular states may be modified, we anticipate that many of our predictions are only weakly affected by these additional states. This is supported by the clear quantitative agreement between the experimentally observed onset of superradiance and the reduced Dicke model [22]. Our findings within the projected subspace may also describe experiments exploiting internal hyperfine states [34], where no higher levels exist.

In addition to the effects of higher-momentum states, one should also note that the intensities of the forward- and backward-propagating pump beams are not of equal magnitude in the experiments of Ref. [22]; they differ by a factor of 0.6 due to losses on reflection. This introduces a coupling to the state $\frac{1}{2}\sum_{\alpha,\beta=\pm}\beta|\alpha k,\beta k\rangle$ which exhibits odd parity under reflection in the pump direction. We expect such contributions to play a similar role to higher-momentum states.

A further source of possible departure from the idealized Dicke model with $g = g'$ arises because of the finite atomic recoil energy. As we demonstrate in Appendix A 2, the processes leading to g and g' correspond to different detunings of the intermediate states, so that $\delta g/\bar{g} = \omega_r(\omega_c - \omega_p)/2(\omega_a - \omega_p)$. We have investigated the possible impact of $g \neq g'$ in Sec. VI B and in Appendix E, where we show that differences $\delta g/\bar{g}$ of the order of 10^{-3} can cause one to cross a phase boundary. However, for the typical values of the detunings used in Ref. [22], this asymmetry is of order $\delta g/\bar{g} \sim 10^{-12}$. It is therefore too small to have any significant effect on our findings. Nonetheless, in experiments with a smaller atom-pump detuning, this asymmetry could play a crucial role.

B. Corrections to semiclassical dynamics

In the above discussion we have focused primarily on the semiclassical dynamics of the effective Dicke model through the solutions of the equations of motion given in Eq. (3). In some places we have also incorporated the leading effect of quantum fluctuations by using Wigner-distributed initial conditions. This may be interpreted as including subleading $1/N$ corrections, where N is the number of atoms [65]. More generally, it would be profitable to investigate the full quantum dynamics governed by the density matrix equations of motion in Eq. (1). However, it is important to bear in mind that since the density matrix describes an ensemble average it will in general mask the effects of spontaneous symmetry breaking. It will also wash out collective and persistent oscillations [81]. Nonetheless, in a single experimental run one still observes spontaneous symmetry breaking [22,23], and the density matrix describes the average over many runs; see, for example, Ref. [82]. In order to recover information on these nontrivial features within the density matrix formulation, one may consider higher-order correlation functions. We leave this problem for future work.

VIII. CONCLUSIONS

In this paper, we have explored the collective dynamics of ultracold atoms in transversely pumped optical cavities. Within the framework of the effective nonequilibrium Dicke model we present a detailed discussion of the rich phase diagram of asymptotic attractors, including steady states, coexistence phases, and regimes of persistent oscillations. We show that the inherent time scales for the destablization of the initial state, and the decay time toward the asymptotic attractors, show strong variations throughout the dynamical phase diagram. Crucially, we have demonstrated that two distinct principal time scales emerge, corresponding to the energy scales ω_0 and ω_0^2/κ. The scale ω_0 characterizes both the typical frequency of collective oscillations and their decay rate for a broad range of parameters. The slower scale ω_0^2/κ governs the decay rate in proximity to dynamical phase boundaries, and may be interpreted as critical slowing down. Most notably, in the regime $\omega < \omega_u$, sweep experiments over 200 ms may be required in order to reach the asymptotic regime. It would be profitable to explore this experimentally, and we discuss the broad implications for finite-duration experiments. In particular, the superradiant phase divides into two distinct regimes, denoted SRA and SRB, with the relaxation rates ω_0^2/κ and ω_0, respectively. From a theoretical perspective it would be valuable to investigate the role of quantum fluctuations and the effects of states outside of the two-level Dicke model description. It would also be interesting to explore the ramifications of these findings in other realizations of the Dicke model.

ACKNOWLEDGMENTS

We are very grateful to K. Baumann, F. Brennecke, and T. Esslinger for helpful discussions of the details of their experiments. We also thank E. Demler, G. Milburn, and S. Sachdev for discussions. M.J.B. and B.D.S. acknowledge EPSRC Grants No. EP/E018130/1 and No. EP/F032773/1. J.K. acknowledges Grants No. EP/G004714/2 and No. EP/I031014/1. This research was supported in part by the National Science Foundation under Grant No. NSF PHY05-51164. M.J.B. acknowledges KITP Santa Barbara for hospitality during the final stages of this work.

APPENDIX A: DERIVATION OF THE GENERALIZED DICKE HAMILTONIAN

Here we provide a derivation of the generalized Dicke Hamiltonian for ultracold atoms placed in an optical cavity, as illustrated in Fig. 1. For simplicity, we consider a homogeneous system, and neglect the effects of the finite beam waist of the pump and cavity fields:

$$\begin{aligned} H = {}& \omega_c \psi^\dagger \psi + \sum_i \left(\omega_a \sigma_i^{ee} - \frac{\hbar^2 \nabla_i^2}{2m} \right) \\ & + \sum_i \left(\sigma_i^{eg} + \sigma_i^{ge} \right) [g_0 (\psi + \psi^\dagger) \cos(k x_i) \\ & + \Omega_f \cos(k z_i - \omega_p t) + \Omega_b \cos(k z_i + \omega_p t)]. \end{aligned} \tag{A1}$$

The Hamiltonian acts on both the center-of-mass position of the atoms and their electronic state. The latter is restricted to the two states involved in the optical transitions, denoted by e and g for the excited and ground states, respectively. In this basis $\sigma_i^{ee} = |e\rangle_i \langle e|_i$ and $\sigma_i^{eg} = |e\rangle_i \langle g|_i$. The sum over i runs over the number of atoms present in the cavity, N. The matter-light interactions correspond to the dipole coupling of the atomic transition to the fields of the cavity and the forward and backward pump fields. The cavity field ψ has explicit quantum dynamics, while the time dependence of the pump fields is externally imposed. The cavity-atom coupling is designated g_0. The pump strengths $\Omega_{f(b)}$ describe the pump beam in the forward (backward) direction, where we allow for imperfect retro-reflection as discussed in Ref. [22] and Sec. VII. We have neglected any difference between pump and cavity wave vectors.

The matter-light coupling in Eq. (A1) contains both co- and counter-rotating terms. The rotating-wave approximation consists of neglecting the counter-rotating terms on the basis that the detuning is large compared to the coupling strengths. This approximation is valid here, since $\omega_c, \omega_a, \omega_p$ are all optical frequencies, and of order 400 THz. This is to be compared to the coupling strengths $\Omega_{f,b}\sqrt{N} \sim g_0\sqrt{N} \sim 1$ GHz. Working in the rotating frame at the pump frequency ω_p and neglecting the counter-rotating terms, the Hamiltonian (A1) can be rewritten in the form $H = H_0 + H_1$, where

$$H_0 = \Delta_c \psi^\dagger \psi + \Delta_a \sum_i \sigma_i^{ee} - \frac{\hbar^2}{2m} \sum_i \nabla_i^2 \tag{A2}$$

and

$$H_1 = \sum_i \left[g_0 \psi \cos(k x_i) + \frac{\Omega_f}{2} e^{ikz_i} + \frac{\Omega_b}{2} e^{-ikz_i} \right] \sigma_i^{eg} + \text{H.c.} \tag{A3}$$

Here $\Delta_c = \omega_c - \omega_p$ is the cavity-pump detuning and $\Delta_a = \omega_a - \omega_p$ is the atom-pump detuning.

As described in Sec. II, the effective Dicke model is a low-energy description within the electronic ground state, valid if the coupling to the electronic excited state is small compared to the detuning Δ_a. As such, one may proceed by making a Schrieffer-Wolff [83] transformation and eliminating the excited electronic state. This gives a transformed Hamiltonian $\tilde{H} = H_0 + (i/2)[S, H_1]$ where $[S, H_0] = i H_1$. One should choose S so that $\tilde{H}$ has no coupling between the resulting dressed electronic states:

$$\begin{aligned} iS = {}& \frac{1}{2} [\Omega_f e^{iz} \hat{f} + \Omega_b e^{-iz} \hat{f}^* + g_0 \psi (e^{ix} \hat{g} + e^{-ix} \hat{g}^*)] \\ & \times \sigma^{eg} - \text{H.c.}, \end{aligned}$$

where, for simplicity, position and momenta are now expressed in units of the cavity wavelength. In addition, we have suppressed the atom labels and the summation. Here the differential operators $\hat{f}$ and $\hat{g}$ are given by

$$\hat{f} = \frac{1}{\Delta_a + \omega_r (1 - 2i\partial_z)}, \quad \hat{g} = \frac{1}{\Delta_a - \Delta_c + \omega_r (1 - 2i\partial_x)},$$

where $\omega_r = \hbar^2 k^2 / 2m$ is the recoil energy. The resulting Hamiltonian has the form

$$\begin{aligned} \tilde{H} = {}& H_0 - \frac{\Omega_f^2}{4} \hat{f} - \frac{\Omega_b^2}{4} \hat{f}^* - \frac{\Omega_f \Omega_b}{8} (\hat{f} e^{-2iz} + \hat{f}^* e^{2iz} + \text{H.c.}) \\ & - \frac{g_0^2}{8} \psi^\dagger \psi [\hat{g}(1 + e^{-2ix}) + \hat{g}^*(1 + e^{2ix}) + \text{H.c.}] \end{aligned}$$

$$-\frac{g_0}{8}\psi^\dagger(\Omega_f e^{iz}+\Omega_b e^{-iz})(\hat{g}e^{-ix}+\hat{g}^*e^{ix})+\text{H.c.}$$
$$-\frac{g_0}{8}\psi(e^{ix}+e^{-ix})(\Omega_f \hat{f}e^{-iz}+\Omega_b \hat{f}^*e^{iz})+\text{H.c.},\tag{A4}$$

where $\hat{f}^*$ and $\hat{g}^*$ denote the *complex* conjugates of the Hermitian operators $\hat{f}$ and $\hat{g}$. In writing Eq. (A4) we have eliminated the excited electronic states, but have made no further approximations. As a result, the form of $\tilde{H}$ is rather unwieldy. In order to expose the resulting behavior we will consider two classes of approximation: the small-recoil approximation $\omega_r/\Delta_a \ll 1$ and the weak-pump approximation $q=\Omega_f\Omega_b/(4\omega_r\Delta_a)\ll 1$. Both of these approximations are valid for the experiments of Ref. [22], and we will now consider each in turn.

1. Small-recoil approximation $\omega_r \ll \Delta_a$

If the recoil energy ω_r is small compared to the atom-pump detuning Δ_a, then one may set $\omega_r=0$ as a first approximation. In this case $\hat{f}\simeq\Delta_a^{-1}$ and $\hat{g}\simeq(\Delta_a-\Delta_c)^{-1}$ become c numbers and the form of Eq. (A4) simplifies considerably. This approximation is well justified for the parameters of Ref. [22] as $\omega_r/\Delta_a\simeq(50\ \text{kHz})/(1\ \text{THz})\sim 5\times10^{-8}$. In this approximation Eq. (A4) becomes

$$\begin{aligned}\tilde{H}=&-\omega_r\nabla^2-\frac{1}{4\Delta_a}\left[\Omega_f^2+\Omega_b^2+2\Omega_f\Omega_b\cos(2z)\right]\\&+\left[\Delta_c-\frac{g_0^2}{\Delta_a-\Delta_c}\cos^2(x)\right]\psi^\dagger\psi\\&-\frac{g_0}{4}\left[\frac{1}{\Delta_a}+\frac{1}{\Delta_a-\Delta_c}\right]\cos(x)\\&\times\left[i(\Omega_f-\Omega_b)\sin(z)(\psi^\dagger-\psi)\right.\\&\left.+(\Omega_f+\Omega_b)\cos(z)(\psi^\dagger+\psi)\right].\end{aligned}\tag{A5}$$

We proceed by introducing a basis set of atomic center-of-mass states for the atoms in their electronic ground state. The first two of these states will correspond to the "spin-down" and "spin-up" states of the effective Dicke model. These basis states are given by the eigenstates of the first line of Eq. (A5), which may be written as

$$\Phi_{\sigma,m,n}(x,z)=\phi_{\sigma,m}(z)\begin{cases}\frac{\cos(nx)}{\sqrt{\pi}}, & n>0,\\ \frac{1}{\sqrt{2\pi}}, & n=0.\end{cases}\tag{A6}$$

The energies are given by $E=\omega_r(n+\varepsilon_{\sigma,m})+\text{const}$, where

$$\frac{d^2\phi_{\sigma,m}}{dz^2}+[\varepsilon_{\sigma,m}-2q\cos(2z)]\phi_{\sigma,m}=0\tag{A7}$$

is the Mathieu equation [84] and $\sigma=\pm$ label the even and odd solutions. The Mathieu parameter $q=\Omega_f\Omega_b/(4\Delta_a\omega_r)$ is a dimensionless measure of the pumping strength. Due to the form of the matrix elements arising from the terms linearly dependent on g_0 in Eq. (A5), not all of the configurations of σ,m,n are coupled. Only those states that can be reached by a sequence of absorption and emission processes, starting from an atom in the ground state, need to be included. If $\Omega_b=\Omega_f$, then only the even Mathieu functions $\phi_{+,m}(z)$ need to be included. However, if $\Omega_b\neq\Omega_f$, the odd Mathieu functions $\phi_{-,m}(z)$ should also be considered.

To recover the effective Dicke model, one must restrict attention to the two lowest states and work in the limit $\Omega_f=\Omega_b=\Omega$. In this case, the lowest coupled states are $\Phi_{+,0,0}$ and $\Phi_{+,1,1}$. The values of the parameters ω,ω_0,U in the effective Dicke model in Eq. (2) can be found by evaluating $\langle\Phi_{+,0,0}|\tilde{H}|\Phi_{+,0,0}\rangle$ and $\langle\Phi_{+,1,1}|\tilde{H}|\Phi_{+,1,1}\rangle$. In terms of the Dicke model parameters in Eq. (2), the energies of a configuration with n_{ph} photons and all N atoms in either their ground or excited states are given by

$$E_{\downarrow,\uparrow}=\mp\frac{\omega_0}{2}N+\left(\omega\mp\frac{UN}{2}\right)n_{\text{ph}}.\tag{A8}$$

By comparing $E_\downarrow$ and $E_\uparrow$ with the expressions for $\langle\Phi_{+,0,0}|\tilde{H}|\Phi_{+,0,0}\rangle$ and $\langle\Phi_{+,1,1}|\tilde{H}|\Phi_{+,1,1}\rangle$, one may identify the coefficients ω, ω_0, and U. We find

$$\omega=\Delta_c-\frac{5g_0^2N}{8(\Delta_a-\Delta_c)},\quad U=-\frac{g_0^2}{4(\Delta_a-\Delta_c)},\tag{A9}$$

where we have carried out the summation over atoms and made use of the results $\langle\Phi_{+,0,0}|\cos^2(x)|\Phi_{+,0,0}\rangle=1/2$ and $\langle\Phi_{+,1,1}|\cos^2(x)|\Phi_{+,1,1}\rangle=3/4$. These coefficients agree with those of Ref. [27] when the pump and cavity frequencies are near detuned. The two-level energy splitting is given by the difference of the eigenvalues of the states written in Eq. (A6), and so

$$\omega_0=\omega_r(1+\varepsilon_{+,1}-\varepsilon_{+,0}).\tag{A10}$$

Evaluating the off-diagonal elements $\langle\Phi_{+,0,0}|\tilde{H}|\Phi_{+,1,1}\rangle$ and equating $\langle\Phi_{+,0,0}|\tilde{H}|\Phi_{+,1,1}\rangle=g\psi^\dagger+g'\psi$, one finds the remaining Dicke model parameters,

$$\begin{aligned}g=g'=&-\frac{g_0\Omega}{2}\left[\frac{1}{\Delta_a}+\frac{1}{\Delta_a-\Delta_c}\right]\\&\times\frac{1}{\sqrt{2}}\int_{-\pi}^{\pi}dz\,\phi_{+,0}(z)\cos(z)\phi_{+,1}(z).\end{aligned}\tag{A11}$$

Up until this point all the results we have derived in Eqs. (A9)–(A11) are formally exact for arbitrary $q=\Omega_f\Omega_b/(4\Delta_a\omega_r)$. However, the fact that one can restrict consideration to the two lowest-momentum states is valid only for weak pumping, i.e., small q. We will therefore focus on the small-q limit; in Appendix A 3 we will return to the general-q case, including also the presence of higher-momentum states. In the small-q limit one obtains

$$\omega_0\approx 2\omega_r,\quad g=g'\approx-\frac{g_0\Omega}{4}\left(\frac{1}{\Delta_a}+\frac{1}{\Delta_a-\Delta_c}\right),\tag{A12}$$

where we have used the approximations $\phi_{+,0}(z)\approx 1/\sqrt{2\pi}$ and $\phi_{+,1}\approx\cos(z)/\sqrt{\pi}$. If one further neglects the cavity-pump detuning Δ_c in comparison to the atom-pump detuning Δ_a, then these expressions reduce to those given in Ref. [22]. In Appendix A 2 we will generalize the results of this section to include the effects of nonzero ω_r/Δ_a.

2. Corrections due to nonzero ω_r/Δ_a

In order to quantify the effects of nonzero ω_r/Δ_a, we return to Eq. (A4), but continue to make use of the $q=0$ approximation used in the second half of the previous section. The main difference that nonzero ω_r introduces is that g and g' are no longer equal. One obtains

$$\begin{aligned} g &= -\frac{g_0\Omega}{4}\left[\frac{1}{\Delta_a+\omega_r-\Delta_c}+\frac{1}{\Delta_a-\omega_r}\right], \\ g' &= -\frac{g_0\Omega}{4}\left[\frac{1}{\Delta_a-\omega_r-\Delta_c}+\frac{1}{\Delta_a+\omega_r}\right], \end{aligned} \tag{A13}$$

where for simplicity we set $\Omega_f=\Omega_b=\Omega$. In the limit $\omega_r\to 0$, these reduce to Eq. (A11). In Sec. VI B, we show that a phase boundary can be crossed if the fractional difference $\delta g/\bar{g}$ is large enough. At leading order in ω_r/Δ_a, the fractional difference given by Eq. (A13) is $\delta g/\bar{g}=\omega_r\Delta_c/\Delta_a^2$. For the experimental parameters in Ref. [22], this fractional difference is too small to cross the phase boundary. However, for smaller Δ_a this fractional difference may become significant.

The results in Eq. (A13) are obtained by the same procedure as in the previous section, by evaluating the off-diagonal matrix element and equating $\langle\Phi_{+,0,0}|\tilde{H}|\Phi_{+,1,1}\rangle = g\psi^\dagger + g'\psi$. In deriving Eq. (A13) we use the basis states $\Phi_{+,0,0}(x,z)=1/(2\pi), \Phi_{+,1,1}(x,z)=\cos(x)\cos(z)/\pi$, which follow from Eq. (A7) at $q=0$. We further employ the identities

$$\begin{aligned} \int_{-\pi}^{\pi}\frac{d\zeta}{2\pi}[\hat{\mathcal{D}}e^{-i\zeta}+\hat{\mathcal{D}}^*e^{i\zeta}]\cos(\zeta) &= \frac{1}{x}, \\ \int_{-\pi}^{\pi}\frac{d\zeta}{2\pi}[e^{i\zeta}\hat{\mathcal{D}}+e^{-i\zeta}\hat{\mathcal{D}}^*]\cos(\zeta) &= \frac{1}{x-2\omega_r}, \end{aligned}$$

where $\hat{\mathcal{D}}=[x-i2\omega_r\partial_\zeta]^{-1}$.

The remaining parameters of the Dicke model are

$$\begin{aligned} U &= -\frac{g_0^2}{4}\left[\frac{1}{\delta+3\omega_r}+\frac{2}{\delta-\omega_r}-\frac{2}{\delta+\omega_r}\right], \\ \omega &= \Delta_c-\frac{g_0^2}{8}\left[\frac{1}{\delta+3\omega_r}+\frac{2}{\delta-\omega_r}+\frac{2}{\delta+\omega_r}\right], \\ \omega_0 &= 2\omega_r-\frac{\Omega^2}{4}\left[\frac{1}{\Delta_a+3\omega_r}+\frac{2}{\Delta_a-\omega_r}-\frac{2}{\Delta_a+\omega_r}\right], \end{aligned}$$

where $\delta=\Delta_a-\Delta_c\equiv\omega_a-\omega_c$. In the limit of $\omega_r\to 0$ these reduce to Eq. (A9) and the small-q expansion of Eq. (A10). These expressions are found using the same procedure as outlined in the previous section, by equating $E_\downarrow$ and $E_\uparrow$ in Eq. (A8) with the expressions for $\langle\Phi_{+,0,0}|\tilde{H}|\Phi_{+,0,0}\rangle$ and $\langle\Phi_{+,1,1}|\tilde{H}|\Phi_{+,1,1}\rangle$. To evaluate these expressions we use the results $\hat{f}|\Phi_{+,0,0}\rangle=(\Delta_a+\omega_r)^{-1}|\Phi_{+,0,0}\rangle$ and $\hat{g}|\Phi_{+,0,0}\rangle=(\Delta_a+\omega_r-\Delta_c)^{-1}|\Phi_{+,0,0}\rangle$ together with

$$\int_{-\pi}^{\pi}\frac{d\zeta}{\pi}\cos(\zeta)\left[\frac{1}{x-i2\omega_r\partial_\zeta}(1+e^{-2i\zeta})+\text{c.c.}+(1+e^{2i\zeta})\frac{1}{x-i2\omega_r\partial_\zeta}+\text{c.c.}\right]\cos(\zeta)=\frac{4}{x-2\omega_r}+\frac{2}{x+2\omega_r},$$

where $x=\Delta_a+\omega_r$ and $x=\Delta_a+\omega_r-\Delta_c$ for integrals involving $\hat{f}$ and $\hat{g}$, respectively.

3. Equations of motion in extended state space

When the parameter q is not small, the restriction to two atomic states is no longer valid. Including higher-momentum states, it is no longer possible to map the problem onto an effective spin Hamiltonian. However, it is still possible to derive a semiclassical description of the coupled atom and cavity system. In this generalized case, the semiclassical description consists of a Gross-Pitaevskii equation for a macroscopically occupied atomic wave function $\chi(x,z)$ coupled to a quasiclassical Heisenberg equation for the photon field ψ.

Decomposing the atomic wave function in some basis $\chi(x,z)=\sum_\alpha\chi_\alpha\Phi_\alpha(x,z)$ and splitting the Hamiltonian into the parts

$$\tilde{H}=h^{(0)}+\psi^\dagger\psi h^{(1)}+(\psi^\dagger+\psi)h^{(2)}+i(\psi^\dagger-\psi)h^{(3)},$$

the explicit equations of motion read

$$\begin{aligned} i\partial_t\chi_\alpha = \big(&M_{\alpha\beta}^{(0)}+|\psi|^2M_{\alpha\beta}^{(1)} \\ &+(\psi^*+\psi)M_{\alpha\beta}^{(2)}+i(\psi^*-\psi)M_{\alpha\beta}^{(3)}\big)\chi_\beta, \end{aligned} \tag{A14}$$

$$i\partial_t\psi=\big(\chi_\alpha^*M_{\alpha\beta}^{(1)}\chi_\beta-i\kappa\big)\psi+\chi_\alpha^*M_{\alpha\beta}^{(2)}\chi_\beta+i\chi_\alpha^*M_{\alpha\beta}^{(3)}\chi_\beta, \tag{A15}$$

where we have defined $M_{\alpha\beta}^{(n)}\equiv\langle\Phi_\alpha|h^{(n)}|\Phi_\beta\rangle$. As long as q is small, one may truncate to two atomic basis states and thereby recover the semiclassical equations in Eq. (3), where $S_z=|\chi_1|^2-|\chi_0|^2$ and $S_x+iS_y=\chi_1^*\chi_0$.

APPENDIX B: FIXED POINTS WITH ARBITRARY g AND g'

In general it is difficult to obtain explicit closed-form expressions for the steady-state solutions of Eq. (3). However, in the special case where $U=0$, simplifications occur for arbitrary g and g'. More generally, for arbitrary U, g, and g', one may obtain self-consistent implicit solutions. We discuss these cases below.

1. $U=0$

In the case where $U=0$, the nonlinear equations become linear equations for the variables ψ_1, ψ_2, S_x, and S_y, where S_z enters via the coefficients. Decomposition of Eqs. (6) and (7) into their real and imaginary parts yields

$$\begin{aligned} \omega_0 S_x &= 2(g+g')S_z\psi_1, \\ -\omega_0 S_y &= 2(g-g')S_z\psi_2, \\ \kappa\psi_1 - \omega\psi_2 &= -(g-g')S_y, \\ \omega\psi_1 + \kappa\psi_2 &= -(g+g')S_x. \end{aligned} \tag{B1}$$

The last two equations may also be written in the form

$$\begin{aligned} (\omega^2+\kappa^2)\psi_1 &= -\omega(g+g')S_x - \kappa(g-g')S_y, \\ (\omega^2+\kappa^2)\psi_2 &= -\kappa(g+g')S_x + \omega(g-g')S_y. \end{aligned} \tag{B2}$$

The condition for nontrivial solutions yields the determinantal self-consistency equation

$$4(g^2-g'^2)^2S_z^2 + 4\omega\omega_0(g^2+g'^2)S_z + (\omega^2+\kappa^2)\omega_0^2 = 0. \tag{B3}$$

This may be solved to yield

$$S_z = \frac{-\omega\omega_0(g^2+g'^2) \pm \sqrt{(2\omega\omega_0 gg')^2 - \omega_0^2\kappa^2(g^2-g'^2)^2}}{2(g^2-g'^2)^2}, \tag{B4}$$

corresponding to a nontrivial superradiant phase with $\psi \neq 0$. In the limit $g = g'$ one obtains $S_z = -\omega_0(\omega^2+\kappa^2)/8\omega g^2$. The critical coupling strength for the onset of superradiance corresponds to $S_z = -N/2$ and is given by

$$g\sqrt{N} = \sqrt{\frac{\omega_0(\omega^2+\kappa^2)}{4\omega}}, \tag{B5}$$

in agreement with the results of Dimer *et al.* [34]. It also coincides with Eq. (11) for the onset of the SRA phase when $U = 0$. The explicit dependence on κ in Eq. (B5) emphasizes that the transition occurs in an open system. In the limit $\kappa = 0$ one recovers the location of the superradiance transition, $g\sqrt{N} = \sqrt{\omega\omega_0}/2$, for the equilibrium Dicke model with counter-rotating terms.

2. $U \neq 0$

In the general case with arbitrary U, g, and g', the steady-state solutions of Eq. (3) are more difficult to obtain in an explicit form. However, one may still obtain self-consistent solutions which relate the photon density to S_z for example. In turn, these implicit consistency equations may be solved numerically. For generic parameters the steady-state equations of motion may be obtained from Eqs. (B1) by replacing $\omega_0 \to \tilde{\omega}_0$ and $\omega \to \tilde{\omega}$, where $\tilde{\omega} \equiv \omega + US_z$, $\tilde{\omega}_0 \equiv \omega_0 + Un$, and $n \equiv |\psi|^2 = \psi_1^2 + \psi_2^2$. For a given photon occupation number, n, nontrivial solutions satisfy the determinantal Eq. (B3) with these replacements. Using the explicit form of $\tilde{\omega} \equiv \omega + US_z$, one obtains a modified quadratic equation for S_z:

$$(\chi^2 - 16g^2g'^2)S_z^2 + 2\omega\tilde{\omega}_0\chi S_z + (\omega^2+\kappa^2)\tilde{\omega}_0^2 = 0, \tag{B6}$$

where we define $\chi \equiv 2(g^2+g'^2) + U\tilde{\omega}_0$. This has solutions

$$S_z = \frac{\tilde{\omega}_0}{\chi^2 - 16g^2g'^2}\left[-\omega\chi \pm \sqrt{16g^2g'^2(\omega^2+\kappa^2) - \kappa^2\chi^2}\right]. \tag{B7}$$

In order to have real solutions to Eq. (B7), one requires $16g^2g'^2(\omega^2+\kappa^2) - \kappa^2\chi^2 \geqslant 0$. This translates into the condition that $\max(0,n_-) \leqslant n \leqslant n_+$ where

$$n_\pm = U^{-2}\left[-2(g^2+g'^2) - U\omega_0 \pm 4gg'\kappa^{-1}\sqrt{\omega^2+\kappa^2}\right].$$

One should restrict attention to those cases where $|S_z| < N/2$. Having found a solution for S_z in terms of the number of photons n, one may also find an equation for n in terms of S_z. Using the analogs of the first two equations in Eq. (B1) with $\omega_0 \to \tilde{\omega}_0$,

$$|\psi|^2 = \psi_1^2 + \psi_2^2 = \frac{\tilde{\omega}_0^2 S_x^2}{S_z^2}\left[\frac{1}{4(g+g')^2} + \frac{r^2}{4(g-g')^2}\right], \tag{B8}$$

where $r \equiv S_y/S_x$. Using the fixed-length spin constraint $\mathbf{S}^2 = N^2/4$, one may eliminate $S_x^2 = (N^2/4 - S_z^2)/(1+r^2)$ in favor of the ratio r. This ratio may be obtained by using the analogs of the first two of Eqs. (B1) to substitute ψ_1 and ψ_2 into the analog of the third equation:

$$r = \mathcal{A}\left(\frac{g-g'}{g+g'}\right), \quad \mathcal{A} = -\frac{\tilde{\omega}_0\kappa}{\tilde{\omega}\tilde{\omega}_0 + 2(g-g')^2S_z}. \tag{B9}$$

Substitution into Eq. (B8) yields

$$n = |\psi|^2 = \frac{\tilde{\omega}_0^2}{4S_z^2}\frac{(N^2/4 - S_z^2)(1+\mathcal{A}^2)}{(g+g')^2 + (g-g')^2\mathcal{A}^2}. \tag{B10}$$

APPENDIX C: LINEAR STABILITY FOR ARBITRARY STATES

In Sec. III C we linearized the equations of motion around the normal ($\Downarrow$) and inverted ($\Uparrow$) states. The corresponding self-consistency equation is given by

$$\begin{vmatrix} \eta + i\kappa - \omega_\mp & 0 & -g & -g' \\ 0 & \eta + i\kappa + \omega_\mp & g' & g \\ \mp gN & \mp g'N & \eta - \omega_0 & 0 \\ \pm g'N & \pm gN & 0 & \eta + \omega_0 \end{vmatrix} = 0. \tag{C1}$$

This yields a quartic equation

$$\begin{aligned} 0 &= \left[(\eta+i\kappa)^2 - \omega_\mp^2\right]\left(\eta^2 - \omega_0^2\right) + (g^2N - g'^2N)^2 \\ &\quad \mp 2\eta(\eta+i\kappa)(g^2N - g'^2N) \mp 2(g^2N + g'^2N)\omega_\mp\omega_0, \end{aligned} \tag{C2}$$

whose roots characterize the possible instabilities. In the case where $g = g'$, Eq. (C2) reduces to Eq. (15). More generally one may linearize the equations of motion in Eq. (3) around an arbitrary state, so that $\psi = \psi_0 + \delta\psi$, $S^- = S_0^- + \delta S^-$, and $S^z = S_0^z + \delta S^z$, one obtains

$$\begin{aligned} \delta\dot{S}^- &= -i\tilde{\omega}_0\delta S^- - iU(\psi_0^*\delta\psi + \psi_0\delta\psi^*)S_0^- \\ &\quad + 2i(g\psi_0 + g'\psi_0^*)\delta S^z + 2i(g\delta\psi + g'\delta\psi^*)S_0^z, \\ \delta\dot{S}^z &= -ig\delta\psi S_0^+ + ig\delta\psi^* S_0^- + ig'\delta\psi S_0^- - ig'\delta\psi^* S_0^+ \\ &\quad - ig\psi_0\delta S^+ + ig\psi_0^*\delta S^- + ig'\psi_0\delta S^- - ig'\psi_0^*\delta S^+, \\ \delta\dot{\psi} &= -(\kappa + i\tilde{\omega})\delta\psi - iU\psi_0\delta S^z - ig\delta S^- - ig'\delta S^+, \end{aligned} \tag{C3}$$

where $\tilde{\omega} = \omega + US_0^z$ and $\tilde{\omega}_0 = \omega_0 + U|\psi_0|^2$. Parametrizing $\delta\psi = ae^{-i\eta t} + b^*e^{i\eta^* t}$, $\delta S^- = ce^{-i\eta t} + d^*e^{i\eta^* t}$, and

$\delta S^z = f e^{-i\eta t} + f^* e^{i\eta^* t}$, one obtains a set of algebraic equations for the coefficients a, b, c, d, and f. The corresponding secular equation is given by $|\eta\mathbb{I} - \mathbb{M}| = 0$, where $\mathbb{I}$ is a 5×5 unit matrix and

$$\mathbb{M} = \begin{pmatrix} \tilde{\omega} - i\kappa & 0 & g & g' & U\psi_0 \\ 0 & -(\tilde{\omega} + i\kappa) & -g' & -g & -U\psi_0^* \\ -2gS_0^z + U\psi_0^* S_0^- & -2g'S_0^z + U\psi_0 S_0^- & \tilde{\omega}_0 & 0 & -2(g\psi_0 + g'\psi_0^*) \\ 2g'S_0^z - U\psi_0^* S_0^+ & 2gS_0^z - U\psi_0 S_0^+ & 0 & -\tilde{\omega}_0 & 2(g\psi_0^* + g'\psi_0) \\ gS_0^+ - g'S_0^- & -gS_0^- + g'S_0^+ & -(g\psi_0^* + g'\psi_0) & (g\psi_0 + g'\psi_0^*) & 0 \end{pmatrix}. \tag{C4}$$

In general, there are in fact only four independent equations owing to the fixed-length constraint $\mathbf{S}^2 = N^2/4$. This is reflected by a redundant zero mode, $\eta = 0$, corresponding to longitudinal fluctuations in the length of the spin. Although Eq. (C4) captures all of the essential information, it is convenient to eliminate this zero mode and use a 4×4 matrix representation for the physical transverse degrees of freedom. Differentiating the fixed-length constraint with respect to time yields $2S^z\dot{S}^z + (S^+\dot{S}^- + S^-\dot{S}^+) = 0$. Linearizing around a fixed point gives $2S_0^z\delta\dot{S}^z + S_0^+\delta\dot{S}^- + S_0^-\delta\dot{S}^+ = 0$, as may be verified by use of Eqs. (C3) and (3). Using the normal-mode parametrization, one obtains the relationship $f = -(S_0^+ c + S_0^- d)/2S_0^z$ between the coefficients. Eliminating f from the linear equations yields $|\eta\tilde{\mathbb{I}} - \tilde{\mathbb{M}}| = 0$, where $\tilde{\mathbb{I}}$ is a 4×4 unit matrix and

$$\tilde{\mathbb{M}} = \begin{pmatrix} \tilde{\omega} - i\kappa & 0 & g - U\psi_0 S_0^+/\left(2S_0^z\right) & g' - U\psi_0 S_0^-/\left(2S_0^z\right) \\ 0 & -(\tilde{\omega} + i\kappa) & -g' + U\psi_0^* S_0^+/\left(2S_0^z\right) & -g + U\psi_0^* S_0^-/\left(2S_0^z\right) \\ -2gS_0^z + U\psi_0^* S_0^- & -2g'S_0^z + U\psi_0 S_0^- & \tilde{\omega}_0 + (g\psi_0 + g'\psi_0^*)S_0^+/S_0^z & (g\psi_0 + g'\psi_0^*)S_0^-/S_0^z \\ 2g'S_0^z - U\psi_0^* S_0^+ & 2gS_0^z - U\psi_0 S_0^+ & -(g\psi_0^* + g'\psi_0)S_0^+/S_0^z & -\tilde{\omega}_0 - (g\psi_0^* + g'\psi_0)S_0^-/S_0^z \end{pmatrix}. \tag{C5}$$

1. Stability of the normal (⇓) and inverted (⇑) states with arbitrary g and g'

In the case of the normal (⇓) and inverted (⇑) states where $\psi_0 = 0$ and $S^z = \mp N/2$, the determinantal equation $|\eta\tilde{\mathbb{I}} - \tilde{\mathbb{M}}| = 0$ reduces to Eq. (C1). This corresponds to the quartic equation given in Eq. (C2). In order to find when the roots become unstable it is convenient to decompose the quartic polynomial into its real and imaginary parts so that $A_\mp(\eta) + iB_\mp(\eta) = 0$ where

$$\begin{aligned} A_\mp(\eta) &= (\eta^2 - \omega_\mp^2 - \kappa^2)\left(\eta^2 - \omega_0^2\right) + (g^2N - g'^2N)^2 \\ &\quad \mp 2(g^2N + g'^2N)\omega_\mp\omega_0 \mp 2\eta^2(g^2N - g'^2N), \\ B_\mp(\eta) &= 2\kappa\eta[\eta^2 - \omega_0^2 \mp (g^2N - g'^2N)]. \end{aligned} \tag{C6}$$

We may thus find the roots of the equation $B_\mp(\eta) = 0$ and subsequently impose the condition $A_\mp(\eta) = 0$ on these solutions. It is readily seen that $B_\mp(\eta) = 0$ has a solution $\eta = 0$ corresponding to an exponentially growing mode without oscillations. Substituting this value into the expression for $A_\mp(\eta)$ yields the condition $A_\mp(0) = 0$:

$$(\omega_\mp^2 + \kappa^2)\omega_0^2 + (g^2N - g'^2N)^2 \mp 2(g^2N + g'^2N)\omega_\mp\omega_0 = 0. \tag{C7}$$

In the special case where $g = g'$ one recovers the critical condition for the onset of the SRA phase as given by Eq. (11). Alternatively, there is also an instability with a finite frequency $\eta^2 = \omega_0^2 \pm (g^2N - g'^2N)$ corresponding to $B_\mp(\eta) = 0$. Demanding that $A_\mp(\eta) = 0$ yields a critical condition for the ratio of the couplings,

$$\frac{g'^2}{g^2} = \frac{(\omega_\mp + \omega_0)^2 + \kappa^2}{(\omega_\mp - \omega_0)^2 + \kappa^2}, \tag{C8}$$

rather than their absolute scales. This instability condition manifests itself as the phase boundaries shown in the upper panels of Figs. 15 and 19. Denoting $\delta g \equiv g' - g$, $\bar{g} \equiv$

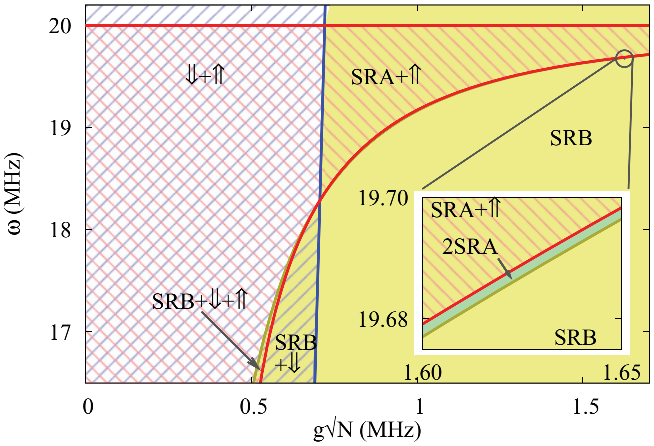

FIG. 17. (Color online) Magnified portion of the bottom panel of Fig. 4 in the vicinity of the tricritical point where three phase boundaries cross. In addition to the phases visible in Fig. 4, there is a narrow region denoted as 2SRA, where the two distinct SRA solutions given by Eq. (10) coexist; see inset.

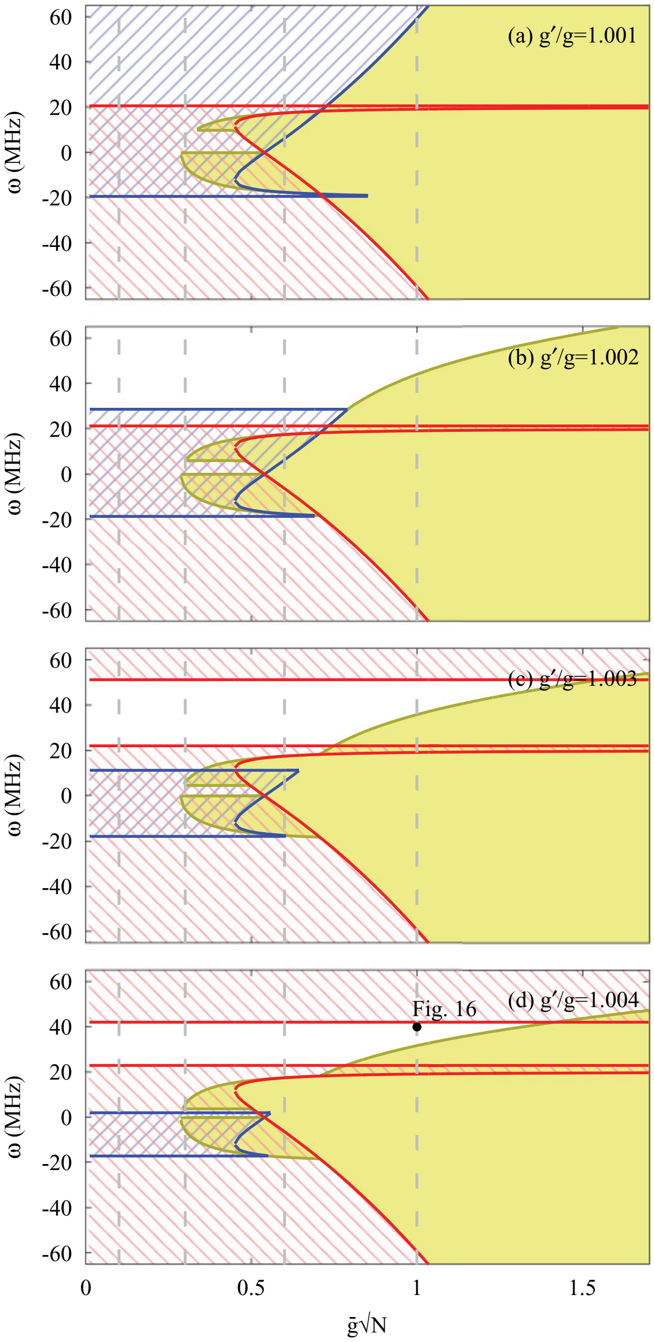

FIG. 18. (Color online) Evolution of the phase diagram shown in the bottom panel of Fig. 4 as one varies the ratio g'/g, increasing from 1.000 (top) to 1.004 (bottom). We use the same phase labeling conventions as in Fig. 4. Vertical dashed lines indicate cuts shown in Fig. 15.

$(g+g')/2$, and noting that $\omega_0 \ll \kappa$, the phase boundary given by Eq. (C8) may be approximated as

$$\frac{\delta g}{\bar{g}} \approx \frac{2\omega_0\omega_\mp}{\omega_\mp^2+\kappa^2}. \tag{C9}$$

In a similar fashion Eq. (C7) may be recast as

$$\bar{g}^2 \approx \frac{(g_a^\mp)^2-\delta g^2/4}{1-\delta g^2 N/\omega_0\omega_\mp}, \tag{C10}$$

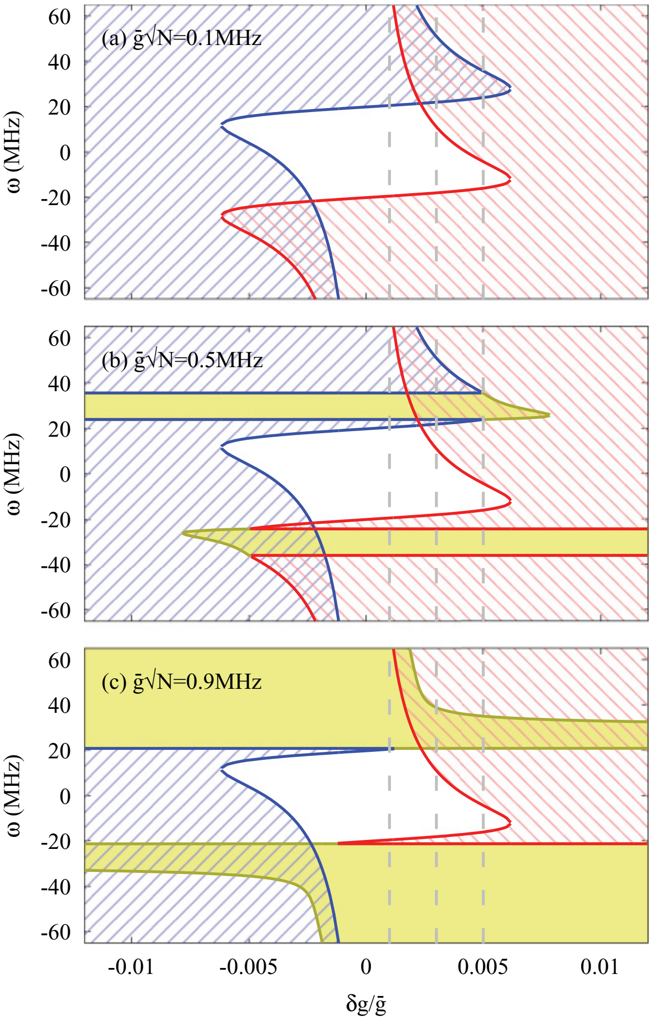

FIG. 19. (Color online) Analog of the phase diagram in Fig. 15 for $UN = +40$ MHz. We use the same phase labeling conventions as in Fig. 4. The panels show the dependence on $\delta g \equiv g' - g$ for fixed $\bar{g} = \frac{1}{2}(g+g')$. The white region corresponds to a regime of persistent oscillations. Vertical dashed lines indicate cuts shown in Fig. 20.

where $g_a^\mp$ is given by Eq. (11). For the range of parameters shown in Figs. 15 and 19, $\delta g \ll \bar{g}, g_a^\mp$, and Eq. (C10) is effectively independent of $\delta g/\bar{g}$; this yields the horizontal phase boundaries in Figs. 15 and 19.

2. Stability of SRA and SRB phases with $g = g'$

When $g = g'$ the SRA phase has $S^y = 0$ and $S^\pm = S^x$. In this case the matrix $\tilde{\mathbb{M}}$ has eigenvalues η, satisfying

$$\begin{aligned}&[(\eta+i\kappa)^2-\tilde{\omega}^2]\big[\eta^2-(\tilde{\omega}_0 N/2S_0^z)^2\big]\\&\quad+\frac{2\tilde{\omega}\tilde{\omega}_0}{S_0^z}|2gS_0^z-U\psi_0S_0^x|^2=0,\end{aligned} \tag{C11}$$

where $\tilde{\omega} = \omega + US_0^z$ and $\tilde{\omega}_0 = \omega_0 + U|\psi_0|^2$.

When $g = g'$ the SRB phase has $\tilde{\omega} = \tilde{\omega}_0 = 0$ and $\psi \equiv \psi_1 + i\psi_2$ is purely imaginary. In this case the diagonal blocks of $\tilde{\mathbb{M}}$ are proportional to unity and zero, respectively. The eigenvalues satisfy Eq. (21) which is the square of a quadratic

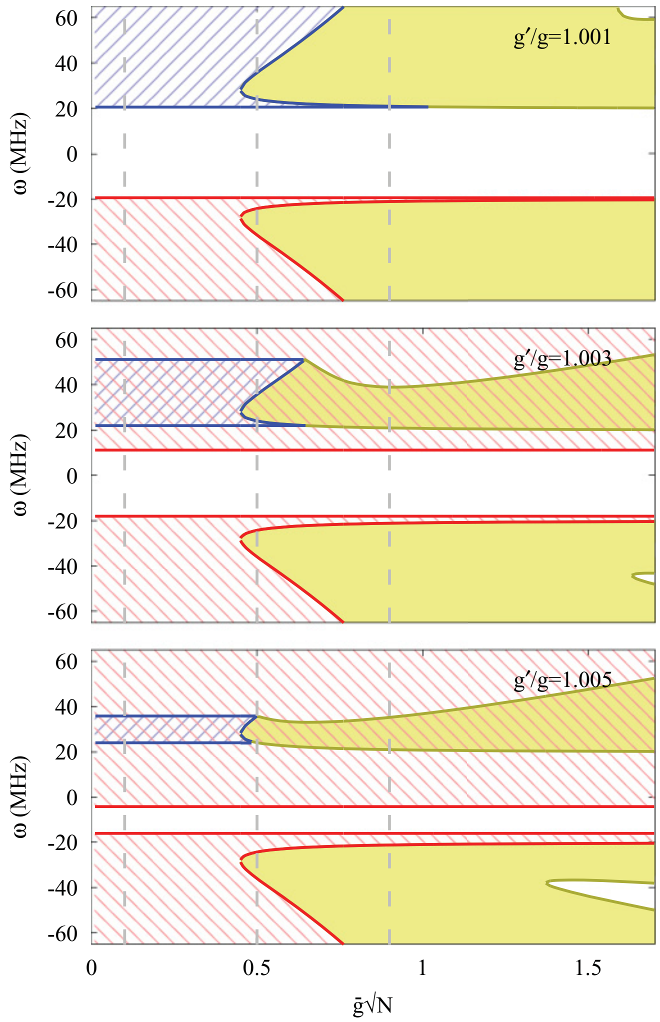

FIG. 20. (Color online) Analog of the phase diagram shown in Fig. 18 for $UN = +40$ MHz. We use the same phase labeling conventions as in Fig. 4. Vertical dashed lines indicate cuts shown in Fig. 19.

equation. The exact eigenvalues corresponding to fluctuations around the stable SRB fixed points are given by Eq. (22).

APPENDIX D: TRANSITIONS NEAR THE TRICRITICAL POINTS

As noted in Ref. [50] for $UN < -2\kappa$, three of the phase boundaries in Fig. 4 cross at the point $\omega = \sqrt{\omega_u^2 - \kappa^2}, g = \sqrt{-\omega_0 U/4}$. As shown in Fig. 17, in this vicinity there is a narrow region where the two distinct SRA solutions given by Eq. (10), together with their parity symmetry partners, are stabilized; see also Fig. 5. On Fig. 4 these occur within the width of the line marking the boundary of the SRA+ $\Uparrow$ and SRB regions. At $g = g_b$ the two pairs of SRA solutions merge and switch to two pairs of SRB solutions. After this, one of each pair is stable while the others are unstable, as generically occurs in the SRB phase.

APPENDIX E: FURTHER CUTS THROUGH THE PHASE DIAGRAM WITH $g \neq g'$ AND $U \neq 0$

In Sec. VI B we presented the dynamical phase diagram with $g \neq g'$ and $UN = -40$ MHz, illustrating the dynamical phase boundaries which emerged for small differences between g and g'. Here we provide further cuts through the phase diagram in order to fully expose the rich topology. In Fig. 18 we show a sequence of cuts with $UN = -40$ MHz for different values of g'/g. These may be compared with the bottom panel of Fig. 4, which has $g'/g = 1$. In view of the duality relation in Eq. (5), we only show the results for $g > g'$. For completeness, in Figs. 19 and 20 we also show cuts of constant $\bar{g} = (g + g')/2$ and g'/g, respectively, with $U = +40$ MHz. The central white region in these figures is continuously connected to the regime of persistent oscillations described in Sec. VI A. We note that the regions where the normal and inverted states are stable have identical shapes to those seen for $U = -40$ MHz in Figs. 15 and 18, respectively, but are displaced vertically.

APPENDIX F: WIGNER DISTRIBUTION

The sampling of initial conditions from a Wigner distribution is readily achieved by combining a Holstein-Primakoff representation for the collective spin operators, $S_z = -N/2 + a^\dagger a$ and $S^- \simeq \sqrt{N}a$ [85,86], with a harmonic oscillator decomposition of the auxiliary bosons, $a = (q + ip)/\sqrt{2}$. The corresponding Wigner distribution $W(q,p) = e^{-q^2-p^2}/\pi$ reflects the Gaussian ground-state wave function of the harmonic oscillator. In terms of the Bloch sphere coordinates with $S^- = (N/2)\sin(\theta)e^{-i\phi}$, this corresponds to $\theta \simeq \sqrt{(q^2 + p^2)/(N/2)}$ and $\phi = -\mathrm{Arg}(q + ip)$. In a similar fashion, the Wigner distribution of the initial photon field $\psi = (Q + iP)/\sqrt{2}$ is given by $W(Q,P) = e^{-Q^2-P^2}/\pi$. In order to employ these ensembles we sample initial conditions from these distributions of (q,p) and (Q,P) and time-evolve the semiclassical equations of motion. We then average the final results over the initial distributions $W(q,p)$ and $W(Q,P)$.

---

[1] F. Brennecke, T. Donner, S. Ritter, T. Bourdel, M. Köhl, and T. Esslinger, Nature (London) **450**, 268 (2007).

[2] Y. Colombe, T. Steinmetz, G. Dubois, F. Linke, D. Hunger, and J. Reichel, Nature (London) **450**, 272 (2007).

[3] T. P. Purdy and D. M. Stamper-Kurn, Appl. Phys. B **90**, 401 (2008).

[4] M. Kohnen, M. Succo, P. G. Petrov, R. A. Nyman, M. Trupke, and E. A. Hinds, Nat. Photonics **5**, 35 (2011).

[5] F. Brennecke, S. Ritter, T. Donner, and T. Esslinger, Science **322**, 235 (2008).

[6] S. Ritter, F. Brennecke, K. Baumann, T. Donner, C. Guerlin, and T. Esslinger, Appl. Phys. B **95**, 213 (2009).

[7] T. P. Purdy, D. W. C. Brooks, T. Botter, N. Brahms, Z.-Y. Ma, and D. M. Stamper-Kurn, Phys. Rev. Lett. **105**, 133602 (2010).

[8] N. Brahms and D. M. Stamper-Kurn, Phys. Rev. A **82**, 041804 (2010).

[9] I. B. Mekhov, C. Maschler, and H. Ritsch, Nat. Phys. **3**, 319 (2007).

[10] W. Chen, D. Meiser, and P. Meystre, Phys. Rev. A **75**, 023812 (2007).

[11] N. Brahms, T. P. Purdy, D. W. C. Brooks, T. Botter, and D. M. Stamper-Kurn, Nat. Phys. **7**, 604 (2011).

[12] S. Leslie, N. Shenvi, K. R. Brown, D. M. Stamper-Kurn, and K. B. Whaley, Phys. Rev. A **69**, 043805 (2004).

[13] A. Wallraff, D. I. Schuster, A. Blais, L. Frunzio, R.-S. Huang, J. Majer, S. Kumar, S. M. Girvin, and R. J. Schoelkopf, Nature (London) **431**, 162 (2004).

[14] D. I. Schuster, A. A. Houck, J. A. Schreier, A. Wallraff, J. M. Gambetta, A. Blais, L. Frunzio, B. Johnson, M. H. Devoret, S. M. Girvin, and R. J. Schoelkopf, Nature (London) **445**, 515 (2007).

[15] P. J. Leek, J. M. Fink, A. Blais, R. Bianchetti, M. Göppl, J. M. Gambetta, D. I. Schuster, L. Frunzio, R. J. Schoelkopf, and A. Wallraff, Science **318**, 1889 (2007).

[16] A. Fragner, M. Göppl, J. M. Fink, R. Bianchetti, P. J. Leek, A. Blais, and A. Wallraff, Science **322**, 1357 (2008).

[17] J. M. Fink, M. Göppl, M. Baur, R. Bianchetti, P. J. Leek, A. Blais, and A. Wallraff, Nature (London) **454**, 315 (2008).

[18] J. M. Fink, R. Bianchetti, M. Baur, M. Göppl, L. Steffen, S. Filipp, P. J. Leek, A. Blais, and A. Wallraff, Phys. Rev. Lett. **103**, 083601 (2009).

[19] L. DiCarlo, M. D. Reed, L. Sun, B. R. Johnson, J. M. Chow, J. M. Gambetta, L. Frunzio, S. M. Girvin, M. H. Devoret, and R. J. Schoelkopf, Nature (London) **467**, 574 (2010).

[20] P. Domokos and H. Ritsch, Phys. Rev. Lett. **89**, 253003 (2002).

[21] A. T. Black, H. W. Chan, and V. Vuletić, Phys. Rev. Lett. **91**, 203001 (2003).

[22] K. Baumann, C. Guerlin, F. Brennecke, and T. Esslinger, Nature (London) **464**, 1301 (2010).

[23] K. Baumann, R. Mottl, F. Brennecke, and T. Esslinger, Phys. Rev. Lett. **107**, 140402 (2011).

[24] A. F. Andreev and I. M. Lifshitz, Zh. Eksp. Teor. Fiz. **56**, 2057 (1969) [Sov. Phys. JETP **29**, 1107 (1969)].

[25] G. V. Chester, Phys. Rev. A **2**, 256 (1970).

[26] A. J. Leggett, Phys. Rev. Lett. **25**, 1543 (1970).

[27] D. Nagy, G. Konya, G. Szirmai, and P. Domokos, Phys. Rev. Lett. **104**, 130401 (2010).

[28] R. H. Dicke, Phys. Rev. **93**, 99 (1954).

[29] K. Hepp and E. H. Lieb, Ann. Phys. **76**, 360 (1973).

[30] Y. K. Wang and F. T. Hioe, Phys. Rev. A **7**, 831 (1973).

[31] C. Emary and T. Brandes, Phys. Rev. Lett. **90**, 044101 (2003).

[32] C. Emary and T. Brandes, Phys. Rev. E **67**, 066203 (2003).

[33] B. M. Garraway, Philos. Trans. R. Soc. London, Ser. A **369**, 1137 (2011).

[34] F. Dimer, B. Estienne, A. S. Parkins, and H. J. Carmichael, Phys. Rev. A **75**, 013804 (2007).

[35] I. Bialynicki-Birula and K. Rzażnewski, Phys. Rev. A **19**, 301 (1979).

[36] P. Nataf and C. Ciuti, Nat. Commun. **1**, 72 (2010).

[37] O. Viehmann, J. von Delft, and F. Marquardt, Phys. Rev. Lett. **107**, 113602 (2011).

[38] J.-Y. Courtois, G. Grynberg, B. Lounis, and P. Verkerk, Phys. Rev. Lett. **72**, 3017 (1994).

[39] R. Bonifacio and L. D. Salvo, Nucl. Instrum. Methods Phys. Res., Sect. A **341**, 360 (1994).

[40] R. Bonifacio, L. De Salvo, L. M. Narducci, and E. J. D'Angelo, Phys. Rev. A **50**, 1716 (1994).

[41] D. Nagy, J. K. Asbóth, P. Domokos, and H. Ritsch, Europhys. Lett. **74**, 254 (2006).

[42] D. Nagy, G. Szirmai, and P. Domokos, Eur. Phys. J. D **48**, 127 (2008).

[43] J. Larson, B. Damski, G. Morigi, and M. Lewenstein, Phys. Rev. Lett. **100**, 050401 (2008).

[44] J. Larson, S. Fernández-Vidal, G. Morigi, and M. Lewenstein, New J. Phys. **10**, 045002 (2008).

[45] S. Gopalakrishnan, B. L. Lev, and P. M. Goldbart, Nat. Phys. **5**, 845 (2009).

[46] Jonathan Keeling, Joe Bhaseen, and Ben Simons, Physics **3**, 88 (2010).

[47] S. Fernández-Vidal, G. De Chiara, J. Larson, and G. Morigi, Phys. Rev. A **81**, 043407 (2010).

[48] S. Gopalakrishnan, B. L. Lev, and P. M. Goldbart, Phys. Rev. Lett. **107**, 277201 (2011) .

[49] P. Strack and S. Sachdev, Phys. Rev. Lett. **107**, 277202 (2011).

[50] J. Keeling, M. J. Bhaseen, and B. D. Simons, Phys. Rev. Lett. **105**, 043001 (2010).

[51] M. O. Scully and M. S. Zubairy, *Quantum Optics* (Cambridge University Press, Cambridge, 1997).

[52] R. Bonifacio and G. Preparata, Phys. Rev. A **2**, 336 (1970).

[53] A. V. Andreev, V. Gurarie, and L. Radzihovsky, Phys. Rev. Lett. **93**, 130402 (2004).

[54] R. A. Barankov and L. S. Levitov, Phys. Rev. Lett. **93**, 130403 (2004).

[55] E. A. Yuzbashyan, B. L. Altshuler, V. B. Kuznetsov, and V. Z. Enolskii, J. Phys. A **38**, 7831 (2005).

[56] E. A. Yuzbashyan, V. B. Kuznetsov, and B. L. Altshuler, Phys. Rev. B **72**, 144524 (2005).

[57] P. W. Anderson, Phys. Rev. **112**, 1900 (1958).

[58] P. R. Eastham, J. Phys.: Condens. Matter **19**, 295210 (2007).

[59] P. R. Eastham, M. H. Szymanska, and P. B. Littlewood, Solid State Commun. **127**, 117 (2003).

[60] J. Keeling, Phys. Rev. A **79**, 053825 (2009).

[61] O. Babelon, L. Cantini, and B. Douçot, J. Stat. Mech. (2009) P07011.

[62] N. Liu, J. Lian, J. Ma, L. Xiao, G. Chen, J.-Q. Liang, and S. Jia, Phys. Rev. A **83**, 033601 (2011).

[63] Numerical Algorithms Group, *The NAG Fortran Library Manual, Mark 22* (The Numerical Algorithms Group Ltd., Oxford, 2009).

[64] A. P. Itin and P. Törma, e-print arXiv:0901.4778.

[65] P. B. Blakie, A. S. Bradley, M. J. Davis, R. J. Ballagh, and C. W. Gardiner, Adv. Phys. **57**, 363 (2008).

[66] S. H. Strogatz, *Nonlinear Dynamics and Chaos* (Perseus Books, Cambridge, MA, 1994).

[67] G. Szirmai, D. Nagy, and P. Domokos, Phys. Rev. A **81**, 043639 (2010).

[68] B. Öztop, M. Bordyuh, Ö. E. Müstecaplıoğlu, and H. E. Türeci, e-print arXiv:1107.3108.

[69] D. Nagy, G. Szirmai, and P. Domokos, Phys. Rev. A **84**, 043637 (2011).

[70] V. M. Bastidas, C. Emary, B. Regler, and T. Brandes, e-print arXiv:1108.2987, Phys. Rev. Lett. (2012).

[71] L. D. Landau and E. M. Lifshitz, Phys. Z. Sowjet. **8**, 153 (1935).

[72] T. L. Gilbert, IEEE Trans. Magn. **40**, 3443 (2004).

[73] H. J. Lipkin, N. Meshkov, and A. J. Glick, Nucl. Phys. **62**, 188 (1965).

[74] N. Meshkov, A. J. Glick, and H. J. Lipkin, Nucl. Phys. **62**, 199 (1965).

[75] A. J. Glick, H. J. Lipkin, and N. Meshkov, Nucl. Phys. **62**, 211 (1965).

[76] S. Morrison and A. S. Parkins, Phys. Rev. A **77**, 043810 (2008).

[77] H. Haken, Rev. Mod. Phys. **47**, 67 (1975).

[78] H. Haken, Phys. Lett. A **53**, 77 (1975).

[79] J. Larson and M. Horsdal, Phys. Rev. A **84**, 021804 (2011).

[80] W. Niedenzu, T. Grießer, and H. Ritsch, Europhys. Lett. **96**, 43001 (2011).

[81] G. J. Milburn, J. Corney, E. M. Wright, and D. F. Walls, Phys. Rev. A **55**, 4318 (1997).

[82] A. J. Leggett, Rev. Mod. Phys. **73**, 307 (2001).

[83] J. R. Schrieffer and P. A. Wolff, Phys. Rev. **149**, 491 (1966).

[84] E. T. Whittaker and G. N. Watson, *A Course of Modern Analysis* (Cambridge University Press, Cambridge, 1952).

[85] T. Holstein and H. Primakoff, Phys. Rev. **58**, 1098 (1940).

[86] A. Auerbach, *Interacting Electrons and Quantum Magnetism* (Springer, Berlin, 1994).